Simulation of Nanoparticle-Stabilized CO_2-Foam in Sandstone

Master Thesis in Reservoir Physics

By

Adam Nour

Department of Physics and Technology

University of Bergen

August 2019

Summary

The numerical study presented in this thesis is a part of an ongoing CO_2-foam project led by the Reservoir Physics group at the Department of Physics and Technology, University of Bergen. The thesis objective was to investigate foam behavior during co-injection of CO_2-brine (baseline) and CO_2-nanofluid using a compositional simulator validated by history matching the experimental results. The compositional simulator GEM provided by The Computer Modelling Group (CMG) was used to perform history matching and sensitivity analysis to investigate how different foam model parameters, including the reference mobility reduction factor (FMMOB), the maximum dry-out parameter (Sfdry), the dry-out slope (Sfbet), absolute permeability, and injection velocity influence foam strength during CO_2 coinjection with and without nanoparticle present.

This thesis focuses on the numerical simulation of CO_2-foam, that involves the foam quality scan of nanoparticles and CO_2 to generate foam for mobility control, and to investigate the foam strength of the nanoparticle-based foam. The numerical simulations were compared with available experimental data from core floods on outcrop Bentheimer sandstone core. The core was fully saturated with brine (no oil) and gas was coinjected with brine and/or nanofluid at different injection rates and gas fractions to generate foam *in-situ*.

An empirical foam model incorporated in the compositional equation-of-state CMG-GEM simulator was utilized. The model included relative permeability and foam model parameters, such as the reference mobility reduction factor (FMMOB), the maximum dry-out parameter (Sfdry) and the dry-out slope (Sfbet). In the experimental work, the maximum apparent viscosity of 7.8 cP was achieved at the optimal gas fraction (f_g = 0.7), whereas, for baseline foam quality scans (without nanoparticles), the apparent viscosity was almost 3 times lower at the same gas fraction for all injection velocities. This indicated foam generation and that nanoparticles were able to stabilize CO_2 foam. The model was capable of reproducing the experimental data with emphasis on the optimal gas fraction, and the apparent viscosity increased to a maximum value (7.7 cP) at the optimal gas fraction for all injection velocities. A near-Newtonian behavior of CO_2-foam was observed both in the experimental data and in the numerical simulations; no shear-thickening behavior (fluid viscosity increases with increasing injection rate) or shear-thinning behavior (fluid viscosity decreases with increasing injection rate) was observed during the foam scanning. The model saturation profiles indicated the foam was generated from CO_2-NP was displacing more water compared to the baseline.

In conclusion, this work provides a methodology for estimating relative permeability and foam model parameters for nanoparticle-stabilized CO_2-foam simulation. The findings will be useful for understanding nanoparticle-stabilized CO_2-foam behavior during foam scanning with and without nanoparticles present. Simulation results showed that the foam apparent viscosity increased during the foam quality scans with nanoparticles present compared to foam quality scans with brine. It was observed that foam model parameters affect water saturation, differential pressure, and apparent viscosity. Finally, simulations revealed that simulation results were in good agreement with experimental data and that nanoparticle-stabilized CO_2-foam has the potential to become a promising method for CO_2 mobility control.

Acknowledgments

This work would not be possibly done without contribution from others. Primarily, I would like to express my sincerest gratitude to my main supervisor **Dr. Zachary Paul Alcorn** and co-supervisors **Prof. Martin A. Fernø** and **Dr. Øyvind Eide** at the Department of Physics and Technology at the University of Bergen, for their guidance, support and positive attitude throughout these years. Thank you for being patient with me and for keeping your doors open whenever I needed your help.

I would also like to thank **Prof. Arne Graue** and **Associate Prof. Geir Ersland** for their contributions to the reservoir physics group.

Furthermore, I would like to thank fellow students in the reservoir physics group for useful discussion and productive working environment.

Finally, I would like to thank my family and friends for their motivation and encouragement. Special thanks go to my parents for their unconventional support, for teaching me good study habits and for believing in me.

Bergen, August 2019

Adam Nour

Table of Contents

Abbreviations

1D	One Dimensional
2D	Two Dimensional
3D	Three Dimensional
AOS	Alpha Olefin Sulfonate
CCS	Carbon Capture and Storage
CCUS	Carbon Capture, Utilization and Storage
CMG	Computer Modelling Group
cP	centi Poise
ECLIPSE	**E**xploration **C**onsultants **L**imited **I**mplicit **P**rogram for **S**imulation **E**ngineering
EOR	Enhanced Oil Recovery
EOS	Equation Of State
e.g.	for example
FCM	First Contact Miscibility
GEM	**G**eneralized **E**quation of State **M**odel Reservoir Simulator
i.e.	in other words
IFT	Interfacial Tension
IMEX	**IM**plicit-**EX**plicit Black Oil Simulator
IOR	Improved Oil Recovery
kPa	Kilopascal
MCF	Million Cubic Feet
MCM	Multiple Contact Miscibility
MMP	Minimum Miscibility Pressure
MMT	Million Metric Tonnes
NCS	Norwegian Continental Shelf
NP	Nanofluid
NaCl	Sodium Chloride
OOIP	Original Oil In Place
ppm	parts per million
PVT	Pressure/volume/temperature
PV	Pore Volume
SAG	Surfactant-Alternating-Gas
STARS	**S**team, **T**hermal and **A**dvanced Process **R**eservoir **S**imulator
Surfactant	Surface active agents
Surf	Surfactant
U.S.	United States
USA	United States of America
WAG	Water-Alternating-Gas
WINPROP	Phase Behavior Analysis tool

Nomenclature

A	Cross-sectional area
CO_2	Carbon Dioxide
D	Core diameter
DJ	Grid block length in the J direction
DK	Grid block thickness in the K direction
F1	Foam function accounts for the effect of surfactant concentration
F2	Foam function accounts for the detrimental effect of oil
F3	Foam function accounts for the effect of flow velocity for shear thinning
F4	Foam function accounts for the effect of flow velocity for the generation effect
F5	Foam function accounts for the effect of oil composition
F6	Foam function accounts for the effect of salt
F7	Foam function accounts for the effect of permeability dependence parameters
FDRY	Foam dry-out function
f_g	Gas fraction
f_Q	Foam quality
FM	Mobility Reduction Factor
FMMOB	Reference mobility factor
K	Absolute permeability
k_{rg}	Relative permeability of gas
k_{rg}^0	Maximum relative permeability of gas
k_{rw}	Relative permeability of water
k_{rw}^0	Maximum relative permeability of water
k_{rwsgi}^0	Water relative permeability at initial gas saturation
k_{ro}	Relative permeability of oil
k_{ro}^0	Maximum relative permeability of oil
L	Length
N2	Nitrogen
n_g	Corey exponent for gas
n_o	Corey exponent for oil
n_w	Corey exponent for water
P_{crit}	Critical pressure
∇P	Pressure gradient
ΔP	Differential pressure
q_f	Volumetric foam rate
q_g	Gas flow rate
q_l	Flow rate of liquid
Q_T	Total injection rate
Sfbet	Dry-out slope
Sfdry	Maximum dry-out value
S_g	Gas saturation
S_g^*	Normalized gas saturation
S_{gi}	Initial gas saturation
S_{or}	Residual oil saturation
S_w	Water saturation
S_w^*	Normalized water saturation
S_{wi}	Initial water saturation
S_{wr}	Irreducible water saturation
T_{crit}	Critical temperature

u_g	The superficial velocity of the gas
u_l	The superficial velocity of the liquid
V_p	Pore volume
%	Percent
Wt.%	Weight percent

$\emptyset$	Porosity
μ	Viscosity
μ_{brine}	Brine viscosity
μ_f	Apparent viscosity of foam
μ_{nf}	Apparent viscosity of no-foam
μ_{app}	Apparent foam viscosity
ρ_{brine}	Brine density
ρ_{CO2}	CO_2 density
ρ_{NP}	Nanofluid density

Chapter 1: Introduction

In order to meet the rising global energy demand in the coming years, several attempts have been made by the governments to find more reliable sources of energy which can be applied for the industry demand i.e. renewable energies, wind and solar energies, hydroelectricity and biomass (EPA, 2018). Using proven resources (i.e., hydrocarbon reserves) more efficiently and economically can meet the growing energy demand. Recently, the production from hydrocarbon reserves has led to a steady decline of the estimated oil in place. Thus, the importance of improving oil recovery is more crucial than ever, and better means of how to recover the remaining oil resources from the known reservoirs are needed.

The use of energy by humans and the dependence on fossil fuels are the main challenges of making a large reduction in greenhouse gas (GHG) emissions. Reduction of GHG has been in focus due to global warming and pollution. The announcement of the Paris agreement sets out a global action plan aimed to limit the global average temperature rise to 2 $°C$ above pre-industrial levels, and limit the CO_2 concentration to 450 ppm by the end of the 21st century (UNFCC, 2015). The concentration of CO_2 in the atmosphere is increasing by approximately 2 ppm per year. In 2016, CO_2 concentration was greater than 400 ppm (Munro *et al.*, 2016). Global energy-related CO_2 emissions reached a historic high in 2018 and point to the challenge of satisfying growing energy demand and other important policy goals while reducing emissions (Equinor, 2019).

An increased focus on the environmental effects of anthropogenic greenhouse gas emissions implies CO_2 utilization and long-term safe storage in hydrocarbon bearing geological formations (Doyle et al., 2018). Carbon (dioxide) capture and storage (CCS) involves the capture of anthropogenic CO_2 at point sources (i.e., fossil fuel based power plant) and its transportation, injection, and storage into subsurface formations (IPCC, 2016). Carbon Capture, Utilization and Storage (CCUS) involves capture, transport, and utilization of anthropogenic CO_2, and ultimately long-term storage of CO_2 for sequestration. CCUS plays a significant role to mitigate CO_2 emissions, especially from the oil and gas industry. CO_2 emissions can be reduced by implementation of CCUS (Hassan *et al.*, 2018). The environmental and economic benefits of CUUS as results of capturing and storing carbon to reduce CO_2 emissions and simultaneously increase oil recovery (Hasan *et al.*, 2015). However, the future deployment of large-scale CCUS will depend mainly on cost reductions for CO_2 separations, and the financial complexity of CCUS projects (Doyle et al., 2018).

On the Norwegian Continental Shelf (NCS), the Equinor Sleipner project is considered to be one of the global pioneers of CCS. The project was the first in the world to use pure CCS technology in a deep saline reservoir (Hardisty et al., 2011). Since 1996 approximately 1 million tonnes per year of CO_2 have been separated from the natural gas and stored into a saline aquifer (the Utsira formation) above the hydrocarbon reservoir zones (Steeneveldt et al., 2006).

CCUS has great potential in the oil and gas industry. CO_2 can be part of multiple enhanced oil recovery techniques. The ongoing projects on CO_2-foam for mobility control (i.e., nanoparticle-stabilized CO_2-foam) as a part of CO_2-EOR aiming to advance the technology of CO_2 foam for anthropogenic CO_2 storage as a part of CCUS. The main problem in CO_2 injection is unfavorable mobility, which leads to poor mobility control of CO_2 in the reservoir. In order to mitigate the poor mobility control of CO_2, foaming agents (i.e., surfactant or nanoparticles) can be added to the co-injected brine to generate foam. Adding nanoparticles to brine solution to control CO_2 mobility and can also potentially stabilize the foam viscosity. The main focus of this thesis is to investigate how to improve CO_2 foam viscosity using nanoparticles as a foaming agent in order to control the mobility of CO_2, which is a challenge in CO_2 injections.

This work presents a simulation investigation on nanoparticle-stabilized CO_2-foam. CO_2 Foam model with an emphasis on physical mechanisms and optimizing parameters using history matching of core data from an earlier experimental study done by the Reservoir Physics Group. The objectives of this thesis were to find end-point gas relative permeability and estimate the different foam model parameters, including the reference mobility reduction factor (FMMOB), the maximum dry-out parameter (Sfdry), and the dry-out slope (Sfbet). Matching of the foam quality scans, which were performed after the co-injections, was undertaken in order to get an estimation for the relative permeability curves and the foam model parameters. A sensitivity study was performed to examine the significance of the parameters on the foam apparent viscosity across the core. Finally, recommendations on possible investigations that will help the modeling of CO_2 foam process were also provided.

This thesis is organized into 5 chapters. Chapter 2 provides a summary of the theory and background that are relevant to this work. Chapter 3 aims to explain the experimental setup behind this work, modeling of relative permeability, modeling of foam parameters, construction of the model, and the strategy of history matching and the sensitivity analysis. Chapter 4 presents the results obtained from the history matching study on CMG-GEM for the baseline foam quality scan (CO_2 and brine) and the foam quality scans of CO_2 and nanoparticles present as a foaming agent. The experimental work was conducted by Rognmo et al. (Rognmo et al., 2017) on Benthiemer sandstone outcrop core and was simulated using CMG-GEM, and the results were compared. The effect of foam on the apparent viscosity was observed in the simulation program. Chapter 5 presents the conclusions of this work based on the simulation study and provides recommendations for future work.

Chapter 2: Theory and Background

2.1 Enhanced Oil Recovery (EOR)

The world's need for oil is increasing due to the growth in energy demand. In other words, industrial societies are dependent on oil and the demand for more energy is increasing every year. All economic measures intended to improve the oil recovery factor are usually defined as Improved Oil Recovery (IOR) methods. IOR measures can be, for example, stimulation of wells, integrated operations, infill drilling, or enhanced oil recovery (EOR) (Lake *et al.*, 2014). Generally, oil recovery can be divided into three stages; primary, secondary and tertiary recovery, where the former two are referred to as conventional recovery methods (Lake *et al.*, 2014) as shown in Figure 1.

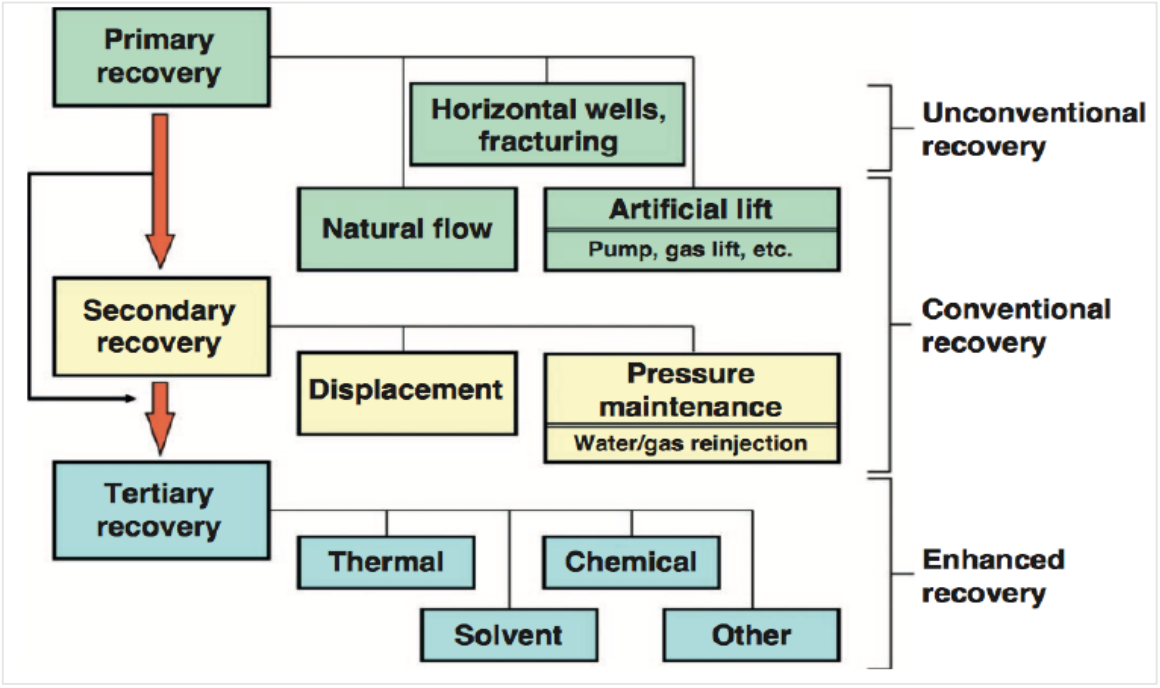

Figure 1: *Classifications of oil recovery methods (Lake et al., 2014).*

In primary recovery, naturally occurring energies (e.g., pressure) with the reservoir are used to drive oil to the surface (Lake *et al.*, 2014). Primary oil recovery results in low ultimate oil recovery due to a rapid decrease in reservoir pressure, which leads to the development of a solution gas drive (Zolotukhin and Ursin, 2000). It is well documented that only a fraction (approximately 10% - 15%) of the oil in place can be recovered with primary recovery (Lake *et al.*, 2014). In secondary recovery, water or gas are injected to improve the sweep efficiency and maintain reservoir pressure (Lake *et al.*, 2014). On the Norwegian Continental Shelf (NCS), the most frequently applied secondary recovery method is water flooding, which has been successful for light oil reservoirs (Zolotukhin and Ursin, 2000). Because of reservoir heterogeneity and unfavorable mobility ratio between the displacing water and oil, the volumetric (macroscopic) sweep efficiency is low. Therefore, waterflooding does not often yield sufficient recovery (Zolotukhin and Ursin, 2000). Primary and secondary recovery together could not recover more than 50% of the original oil in place (OOIP) (Kokal and Al-Kaabi, 2010).

Enhanced oil recovery (EOR) or tertiary recovery incorporates advanced processes of hydrocarbon production (Lake *et al.*, 2014), where additional hydrocarbons are produced by injecting fluids and

energy not initially present in the reservoir. The focus has been mainly on EOR as a tertiary recovery process. However, EOR is not restricted to a specific phase of production. Gas injection, Water-Alternating-Gas (WAG), Surfactant-Alternating-Gas (SAG), chemical flooding (polymers, surfactants), and thermal methods (steam injection, in-situ combustion, hot waterflooding) are the main EOR techniques (Lake *et al.*, 2014). EOR targets the residual trapped oil in both swept and un-swept regions of the reservoir. The total oil displacement efficiency is dependent on microscopic and macroscopic displacement efficiencies. An EOR process can increase the microscopic efficiency, by achieving a low and more favorable interfacial tension between displacing and displaced fluid, yielding mobilization of capillary trapped oil (Lake *et al.*, 2014). The macroscopic efficiency can be improved by reducing oil viscosity and by achieving a favorable mobility ratio between the displacing and displaced fluids. This thesis will focus on pure CO_2 injection and CO_2 foam with and without nanoparticles as an EOR method.

Carbon Dioxide Enhanced Oil Recovery

CO_2 injection is one of the most effective methods to enhance oil recovery from petroleum reservoirs, especially from depleted reservoirs, where the liberation and expansion of gas as a consequence of oil production and pressure decline is the primary source of energy in the reservoir (Lake *et al.*, 2014). CO_2 injection can be employed as a secondary and tertiary EOR method (Zhang *et al.*, 2015; Ahmadi *et al.*, 2016). CO_2 is one of the best hydrocarbon extraction solvent, which makes it an attractive option to enhance oil recovery (Enick *et al.*, 2012). For more than 40 years in conventional reservoirs, CO_2 has been successfully employed, mainly in regions with abundant CO_2 sources (e.g., the Permian Basin and Williston Basin in the USA) (Alvarado and Manrique, 2010). In 2012, CO_2 floodings into sandstone and carbonate formations were able to produce around 280,000 barrels of oil per day, just over 5% of total U.S. crude oil production (Enick *et al.*, 2012; Zhang *et al.*, 2019). Associated CO_2 capture can also help reduce carbon emissions from power plants and other industrial processes that generate large quantities of CO_2.

CO_2 consists of two oxygen atoms and one carbon atom. It can form a liquid or supercritical phase at typical reservoir temperature and pressure conditions, and its critical pressure (P_{crit}) is 73.8 bar, and critical temperature (T_{crit}) is 31.1^{o}C. When reservoir temperature and pressure are above critical thresholds, CO_2 is called ''supercritical''. In comparison with other gases, CO_2 has significant variations in viscosity and density close to the critical point. This can make the displacement front more stable during CO_2-EOR injection. Moreover, supercritical CO_2 gas viscosity and density close to that of a liquid reduce the gravity drainage effect in comparison with other gas injections (Rossen *et al.*, 2007; Fredriksen, 2018). By achieving miscibility of CO_2 with the reservoir fluids, the interfacial tension (IFT) becomes negligible resulting no oil trapped by capillary forces and implies that the residual oil saturation can be reduced to almost zero during CO_2 miscible flood. The volume of the oleic phase can also be increased if the injected gas mixes with and/or dissolved into reservoir oils. This yields more oil production due to the swelling effect combined with pressure surge (Holm and Josendal, 1974; Yellig and Metcalfe, 1980).

CO_2 Emissions

Increasing greenhouse gas emissions in the atmosphere is becoming a significant concern worldwide. A global effort has been undertaken in the announcement of Paris agreement to limit the average temperature rise to 2 $^{\circ}C$ and limit the CO_2 concentration to 450 ppm by the end of the 21st century (UNFCC, 2015). Billions of tons of carbon in the form of CO_2 are absorbed by oceans and living biomass (e.g., sinks) and are emitted to the atmosphere annually through natural processes (e.g., sources) (EPA, 2018). In equilibrium, global carbon fluxes among these various reservoirs are roughly balanced. The global atmospheric concentrations of CO_2 have risen approximately 45 percent since the Industrial Revolution in the late 1700s. This is due to the combustion of fossil fuels for energy. In 2017, fossil fuel combustion in the U.S. accounted for 93.2 percent of CO_2 domestic emissions (EPA, 2018).

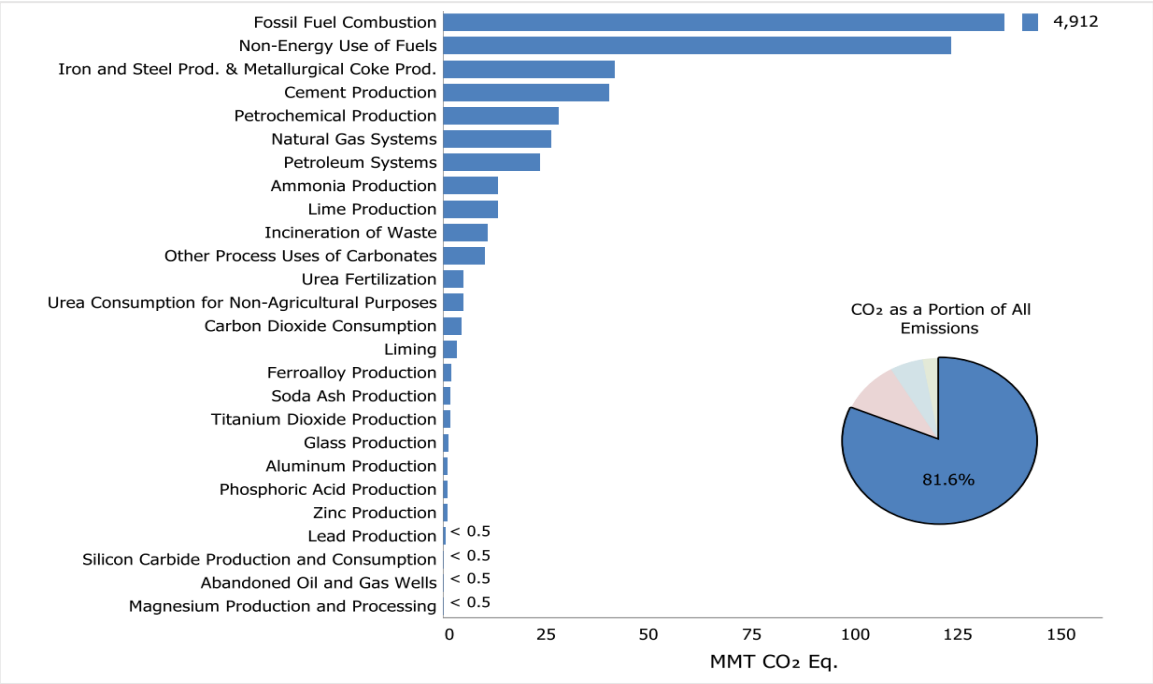

Figure 2: *Sources of CO_2 emissions, where CO_2 from fossil fuel combustion is the largest source of U.S. greenhouse gas emissions, which has increased from 4738.8 MMT CO_2 Eq. to 4912.0 MMT CO_2 Eq., a 3.7 percent total increase between 1990 and 2017. Conversely, these emissions decreased by 49.9 MMT CO_2 Eq. (1.0 percent) from 2016 to 2017. There are 25 additional sources of CO_2 emissions included in this inventory. CO_2 in blue, representing approximately 81.6 percent of total greenhouse gas emissions, which was primary greenhouse gas emitted by human activities in the U.S. (EPA, 2018).*

In 2016, approximately 32,310 million metric tons (MMT) of CO_2 equivalents were added to the atmosphere through fossil fuels combustion worldwide, of which the U.S. accounted for approximately 15 percent. Figure 2 illustrates the sources of CO_2 emissions as the following (EPA, 2018);

- CO_2 emissions from fossil fuel combustion, which increased from 4739 MMT CO_2 Eq. to 4.912 MMT CO_2 Eq. (3.7 %) between 1990 and 2017. From 2016 to 2017, these emissions decreased by 49.9 MMT CO_2 Eq. (1.0 %) and they are the largest source of U.S. greenhouse emissions.
- CO_2 emissions from non-energy use of fossil fuels, which increased by 3.7 MMT CO_2 Eq. (3.1 %) from 1990 through 2017.
- CO_2 emissions from iron and steel production and metallurgical coke production, which have decreased by 59.8 MMT CO_2 Eq. (58.9 %) from 1990 through 2017, due to the restructuring of the industry and increased scrap steel utilization.

There are 23 additional sources of CO_2 emissions included in the study (see Figure 2). Although not illustrated in Figure 2, forestry practices and changes in land use can also lead to net CO_2 emissions or to a net sink of CO_2 (e.g., through net additions to forest biomass) (EPA, 2018). Different approaches are considered and adopted by various countries to mitigate their CO_2 emissions, including (Leung *et al.*, 2014);

- Switch to less carbon-intensive fuels (coal to natural gas).
- Increase the energy efficiency of industrial processes.
- Increase the capacity of biological sinks (e.g., afforestation and agriculture).
- Increase energy production from renewable (e.g., solar, wind and hydro) and nuclear sources.
- Addition of carbon capture and storage (CCS) capability to fossil-fuel-based power sources and energy-intensive industries.

CO_2 Miscibility

For petroleum reservoirs, miscibility can be defined as the physical condition between two or more fluids that will permit them to mix in all proportions (Holm, 1986). Miscible CO_2 injection is a vital EOR process, and it is a proven technology targeting light to medium oils. Since 2012, CO_2 miscible flooding has become the most productive EOR method in the United States (Zhang *et al.*, 2019). Depending on the reservoir pressure and temperature, two types of miscible flooding can occur; first-contact miscibility (FCM) where oil and gas miscible when mixed in all portions, or miscibility can also be developed by a multiple-contact (MCM) process (Bahadori, 2018).

The pressure at which miscibility occurs is defined as minimum miscibility pressure (MMP) (Bahadori, 2018). CO_2 MMP is determined by pressure, temperature, solvent purity, and molecular weight of the heavy fractions of the reservoir oil (Lake *et al.*, 2014). In order to achieve optimal recovery of the residual oil in the reservoir, CO_2 pressure has to be equal or higher than MMP. In an oil reservoir, the composition of the crude oil may influence CO_2 miscibility (Zhang *et al.*, 2015; Wei *et al.*, 2017).

Another critical parameter for oil recovery is the CO_2 solubility. Solubility is the ability of a limited amount of one substance to mix with another substance to form a single homogeneous phase (Holm, 1986). CO_2 solubility in the brine or oil phase is an important parameter that can affect EOR processes. CO_2 solubility in crude oil is mainly controlled by saturation pressure, temperature, and API gravity. CO_2 solubility increases with pressure and API gravity and decreases with a rise in temperature. At supercritical CO_2 condition, CO_2 dissolves in oil as a gas rather than as a liquid. This consequently affects oil viscosity, density, and interfacial tension (IFT) (Bahadori, 2018). CO_2 solubility in the oil phase results in oil viscosity reduction and swelling, which consequently, enhances the oil recovery (Blunt *et al.*, 1993). A better understanding of solubility and its effects on oil recovery and CO_2 storage mechanisms plays an essential role in the success of CO_2-based EOR and CO_2 storage projects (Mosavat *et al.*, 2014).

Benefits of CO_2 injection

The most prominent advantage of CO_2 injection is reducing greenhouse gases in the atmosphere and consequently reducing environmental problems such as global warming. The purpose of CO_2 injection is mainly to improve microscopic sweep (Ahmadi *et al.*, 2016). When CO_2 and reservoir oil are mixed, two physical changes occur, leading to enhanced oil recovery. First, the CO_2-oil mixture has a lower viscosity than the original oil, which makes it easier for the contacted oil to flow in the porous medium. Second, the high CO_2 solubility in oil causes the oil to swell (Holm and Josendal, 1974; Do and Pinczewski, 1993). Oil swelling has a positive impact on oil recovery, as it mobilizes the remaining oil by increasing the oil saturation, and hence, the oil relative permeability also increases (Do and Pinczewski, 1993). The vertical sweep efficiency can also be improved because CO_2 density is lower than oil so it will move towards the top of the reservoir and it can sweep areas that the water did not sweep (Wang *et al.*, 2018). During miscible flooding, CO_2 can extract heavier crude oil components up to C_{30} compared to hydrocarbon gases, such as lean gas, which can only extract intermediate components, C_2-C_6 (Skjæveland, SM and Kleppe, J., 1992). It can also achieve pressure maintenance, but it is not considered as an EOR method.

Challenges of CO_2 injection

There are a number of challenges with gas injection. First and foremost is that the overall sweep efficiency is reduced due to early gas breakthrough during immiscible CO_2 flooding. Typically it takes about 10 MCF of CO_2 to recover an incremental barrel of oil, causing large quantities of effluent CO_2 that that must be separated from the hydrocarbons, re-pressurized and re-injected (Pope, 2011). In reservoirs with good vertical communication between layers, gravity override (Figure 3c) occurs due to the low density of CO_2, where CO_2 can segregate to the top of pay zones (Fredriksen, 2018). The low CO_2 viscosity compared to water and oil results in viscous fingering (Figure 3a) (Lake *et al.*, 2014). Gas channeling (Figure 3b) can lead to early CO_2 breakthrough at the producer and low incremental oil recoveries (Fredriksen, 2018). Moreover, flow assurance issues where gas and water under specific temperature and pressure conditions form hydrates, or asphaltene precipitation from the oils during gas injection (Panuganti *et al.*, 2012). The reservoir heterogeneities can also lead to poor sweep efficiency and bypass of uncontacted oil (J. S. Kim *et al.*, 2005). However, in many shallow reservoirs, the pressure is below the minimum miscibility pressure (MMP) for efficient CO_2 displacement. This remaining crude oil usually is not a target of CO_2 floods (Hirasaki *et al.*, 2015).

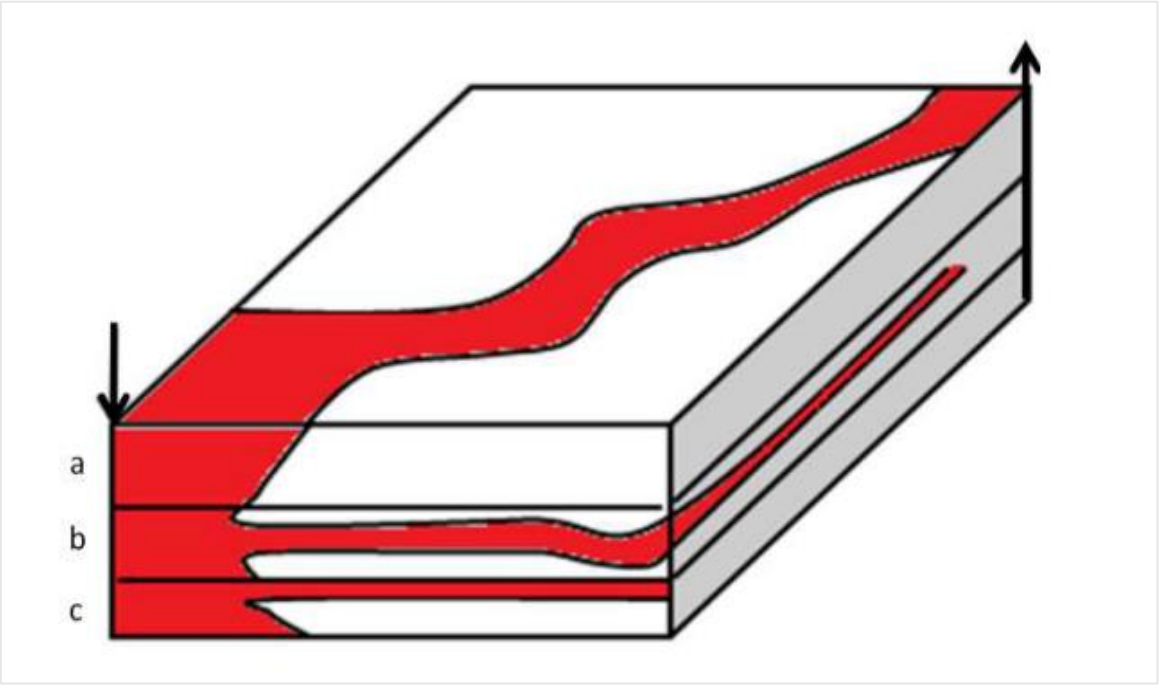

Figure 3: *Problems caused by high CO_2 mobility in a reservoir. In gas injection; a) viscous fingering, which occurs due to low gas viscosity compared to the viscosity of the oil and as a result an unstable displacement front will be created (Fredriksen, 2018), b) gas channeling due to high-permeability regions which lead to rapid gas breakthrough and poor vertical displacement efficiency , and c) gravity override, which occurs as a result of gravity forces and density contrasts between injected and displaced fluid (Zolotukhin and Ursin, 2000). CO_2 injected in red and reservoir matrix in white (Alcorn, 2018).*

2.2 CO_2 Foam Enhanced Oil Recovery

CO_2 foam EOR shows improvement in both vertical and aerial sweep efficiencies by reducing CO_2 mobility and reducing the effect of reservoir heterogeneity (Lee and Kam, 2013). CO_2 foam has great potential to improve oil production. Foams block the high-permeable zones to divert injected gas to lower permeability zones, thereby improving sweep efficiency, and stabilizing the displacement process. The major challenge associated with the gas injection is its poor volumetric sweep efficiency, as a result of which gas does not contact a significant fraction of the reservoir, therefore, the overall recovery remains low (see Figure 4) (Farajzadeh *et al.*, 2012). Foam affects oil recovery in two ways; (1) stabilize the displacement process by increasing gas viscosity and (2) diverting gas toward upswept zones to reach remaining and trapped oil left behind the water-flood. Increasing oil recovery by increasing the capillary number is the primary goal of any recovery method. Increasing the capillary number can be done in two ways; increasing gas viscosity and reducing interfacial tension (IFT) (Farajzadeh *et al.*, 2010).

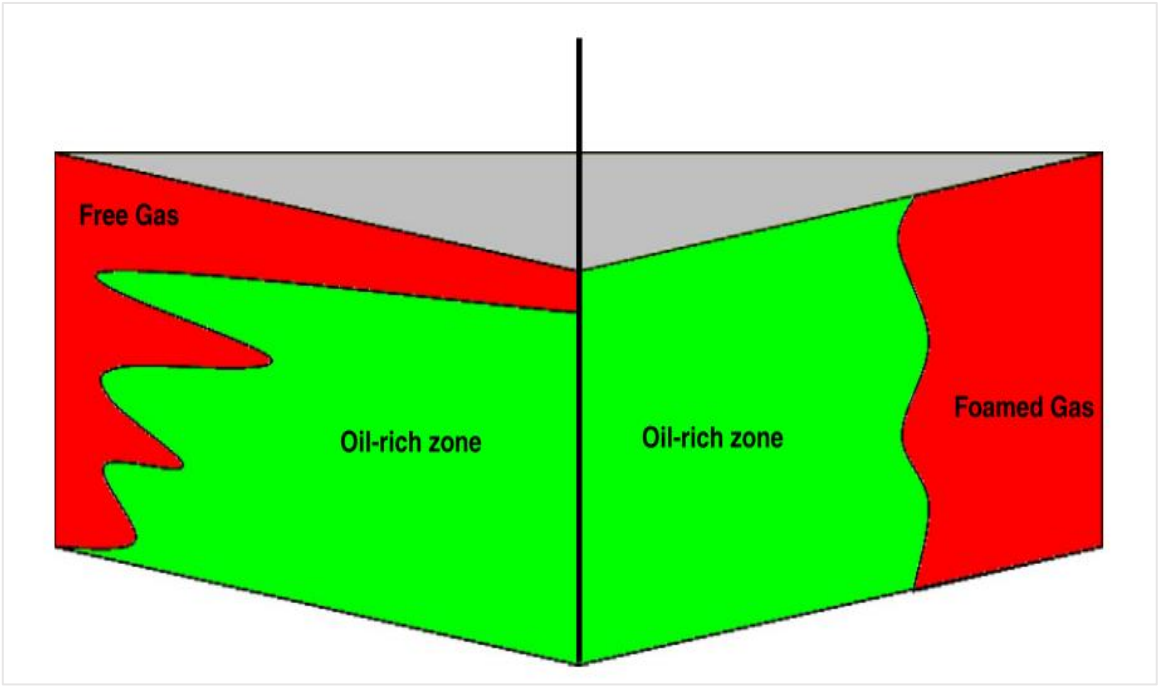

Figure 4: *Schematic showing gas flooding vs. foamed gas flooding (Farajzadeh et al., 2012).*

In a porous media, foam can be defined as a gas-liquid dispersion, where the liquid is the continuous phase, and gas is the discontinuous phase (David and Marsden Jr, 1969). The liquid phase consists of water or a water/hydrocarbon mixture (Gauteplass *et al.*, 2015), while the most common gas phases used in petroleum engineering are N_2, CO_2 and hydrocarbon gas (HC). The gas phase is contained inside the liquid phase in multiple bubbles that are separated by thin liquid film defined as lamellae, illustrated in Figure 5. The connection of three lamellas at an angle of 120^o is referred to as the plateau border (Lake *et al.*, 2014). Lamellae stabilized by adding surface-active agents (surfactants) or nanoparticles (nanoparticles applied in this thesis) to the aqueous phase or to the CO_2 (Laurier L Schramm, 1994; Enick *et al.*, 2012). There are two types of foam: wet foam and dry foam. A foam comprising spherical bubbles separated by thick layers of liquid is referred to a wet foam, whereas foam bubble with the polyhedral shape is referred to dry or strong foam, where lamellae separated the discontinuous gas phase (Chang and Grigg, 1999; Sheng, 2013a).

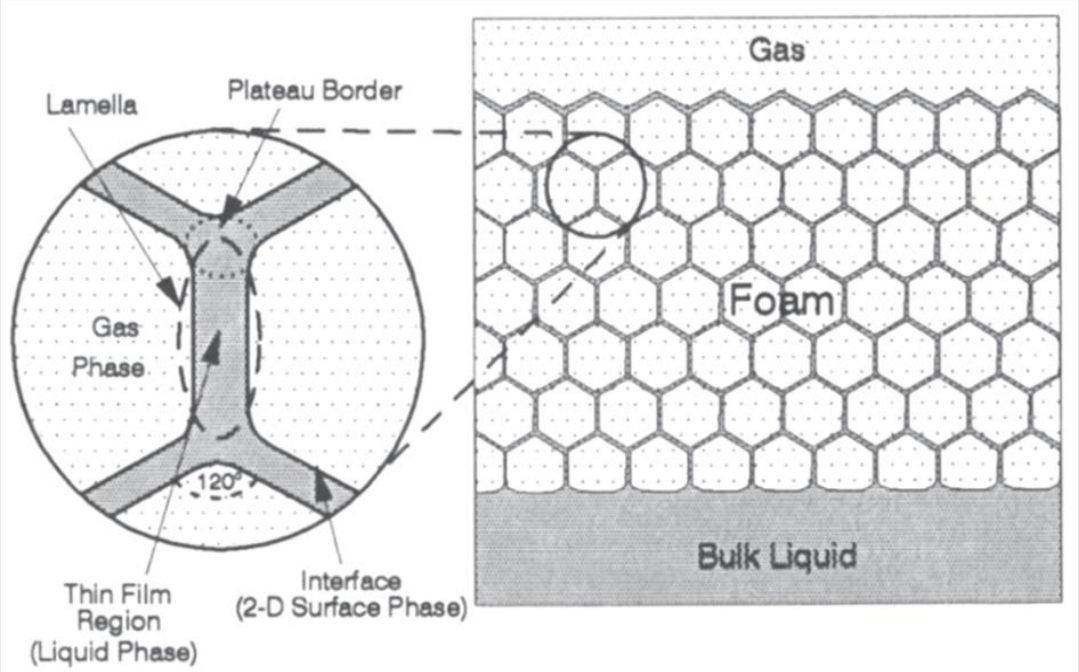

Figure 5: *Bulk foam structure comprising thin liquid lamellae connected in Plateau borders (Laurier Lincoln Schramm, 1994).*

2.2.1 CO_2 Foam Generation

Foam in porous media is generated during the co-injection of gas and foaming agent (surfactant or nanoparticle) solution. Foam can also be generated during the injection of CO_2 and surfactant as alternating (e.g., SAG). There are three methods of lamellae creation, illustrated in Figure 6; (a) leave-behind, (b) capillary snap-off, and (c) lamellae division (Ransohoff and Radke, 1988).

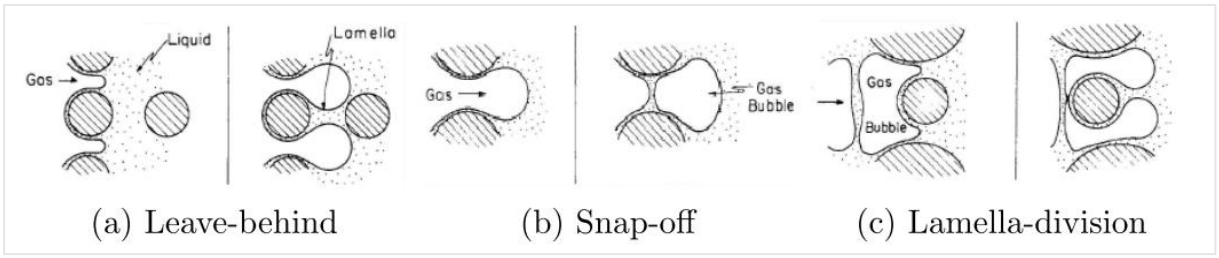

Figure 6: *Illustration of Lamella creation mechanisms. a) Leave-behind mechanism occurs when CO_2 enters a pore-throat opposite direction, b) Snap-off mechanism is the swelling of wetting-films at pore-throats, and c) Lamella division when the CO_2 bubble passes through pore-throats to create new bubbles(Ransohoff and Radke, 1988).*

Leave-behind lamellae (Figure 6a) begin as two gas fronts from different directions approach the same pore space filled with liquid. The liquid in the pore space will then be squeezed into a lamella by the two gas fronts. Gas pathways are blocked, as this mechanism creates a large number of lamellas, resulting in a reduction in gas relative permeability and increased resistance to gas flow. The amount of leave-behind lamellas depends on the coordination number of a pore. This form of lamella creation occurs only during the drainage-like process (CO_2 saturation increases across the pore-network). Hence, the foam generated by leave-behind mechanism is weak due to not forming separate gas

bubbles, where gas remains as a continuous phase (Ransohoff and Radke, 1988; Ettinger and Radke, 1992; Rossen, 1999).

Snap-off mechanism (Figure 6b) occurs when gas (non-wetting phase) displaces liquid in pore space and flows through a narrow pore throat. The snap-off of a gas bubble occurs when the capillary pressure decreases as the gas bubble expands, and the differential pressure across the gas-liquid interface at the pore throat is more significant than at the leading interface (Ransohoff and Radke, 1988). Discontinuity in the flowing gas phase is increased, and lamellae are generated (Dicksen *et al.*, 2002). The foam bubbles block the pathway of the flowing gas and result in a decrease in gas permeability. This mechanism is considered the main mechanism for foam generation in porous media and leads to generate a strong foam in the presence of a foaming agent (i.e., surfactants) (Ransohoff and Radke, 1988; Chen et al., 2010; Liontas et al., 2013; Gauteplass et al., 2015).

Lamella-division mechanism (Figure 6c) is denoted as a secondary foam generation as it only occurs when the foam is already present and flow in the porous media (Ransohoff and Radke, 1988). When a moving lamella approaches a branch point in the field of flow, the leading front (lamella and gas) can flow either into two or more channels, generating new lamellae (Dicksen *et al.*, 2002). Lamella division is repeated several times at the same point, where bubbles may either flow through the media or block the gas pathway (Sheng, 2013a). Sufficient lamella division may render the CO_2 phase discontinuous, resulting in a significant reduction in CO_2 mobility at constant flow conditions (Fredriksen, 2018).

2.2.2 CO_2 Foam Stability

CO_2 foam stability is dependent on the stability of the lamellae. Foam is thermodynamically unstable, and eventually, it collapses, so it is essential to predict the foam stability (Gauglitz *et al.*, 2002). An effective foaming agent is needed in order to make sure that foam remains stable in the reservoir over distance and time (Farajzadeh *et al.*, 2012). Film thinning and coalescence (film rupturing) are two processes that can be related to foam stability (Schramm, 1994). There are several factors that influence the stability of the foam, including properties of the foam film and the petrophysical properties of the porous media (Sheng, 2013a). Some of these factors are bubble size diffusion, pressure, temperature, capillary pressure, liquid viscosity, the presence of oil, and foaming agent (surfactant and/or nanoparticle) (Schramm, 1994; Sheng, 2013b; Lake *et al.*, 2014).

Effect of oil saturation on foam stability

Foam stability depends on the oil saturation in the formation. Oil can destroy aqueous foams, depending on the foaming agent formulation, compositions of the oil and gas, pressure, and temperature (Schramm, 1994; Rossen, 1996). Oil spreading on the water/gas interface is believed to be a significant mechanism of foam destruction by oil (Lee and Kam, 2013). The previous laboratory studies focused on a limiting oil saturation for foam stability, above which no foam could form (Lake *et al.*, 2014). Oil can reduce foam stability by changing the surface tension at the film surfaces (Farajzadeh *et al.*, 2012). When oil droplets enter into the foam lamella and spread on the gas-liquid interface, the gas-water interface becomes a gas-oil interface, which changes interfacial forces and makes lamella unstable (Farajzadeh *et al.*, 2012; Sheng, 2013a). Foam stability in the presence of oil has been found to be related to the molecular weight of the oil molecule (Schramm, 1994). Foam generation and stability can possibly be connected to the foaming agent's ability to solubilize oil molecules (Farajzadeh *et al.*, 2012). Oil destabilizes foam when it creates emulsions. The foam seems

to be destabilized most by oil consists of light components (Schramm, 1994). Foam injection with intermediate to low tolerance for oil may be sufficient for mobility control in swept regions where the oil saturation is low (Sheng, 2013a). If the foam is destroyed, apparent foam viscosity decreases due to that capillary forces dominated over the viscous forces, and oil remains trapped (Farajzadeh *et al.*, 2010).

2.2.3 CO_2 Foam Flow Behavior

In porous medium, foam does not alter water relative permeability or liquid viscosity. However, foam reduces gas mobility significantly (Liu et al., 2011). There are several methods to describe the foam flow behavior in porous media, such as foam quality, apparent foam viscosity, and the foam mobility reduction factor (Sheng, 2013a).

CO_2 Foam Quality

Foam is generally characterized by foam quality and bubble size. Both are essential factors that affect the behavior of the foam flow (Sheng, 2013a). In Eq. (2.1), foam quality (f_Q) is defined as the ratio of gas volumetric flow rate (q_g) and the sum of the total volumetric flow rate of liquid and gas $q_l + q_g$ multiplied by 100 percent (Farajzadeh *et al.*, 2012). The unit for foam quality is the percentage (%).

$$f_Q = \frac{q_g}{q_l + q_g} \times 100\% \tag{2.1}$$

CO_2 Foam Apparent Viscosity

The foam viscosity is much higher compared to both water and gas (Bertin *et al.*, 1998). The apparent foam viscosity (μ_{app}) is defined as the relationship between flow rate and pressure drop for foam flow through a capillary (Friedmann and Jensen, 1986; Chang and Grigg, 1999). Apparent viscosity can be calculated using Darcy's law, considering foam as a single fluid:

$$\mu_{app} = \frac{kA\Delta p}{q_f L} \tag{2.2}$$

Where μ_{app} is the apparent viscosity, k is the absolute permeability, A is the cross-section to the flow rate, Δp is the differential pressure across the capillary, q_f is the volumetric foam rate, and L is the length of the capillary (Svorstol *et al.*, 1996). Equation (2.2) can be modified in terms of pressure gradient and superficial velocities of gas and liquid and can be rewritten as equation (2.3):

$$\mu_{app} = \frac{k\nabla P}{u_g + u_l} \tag{2.3}$$

where k is the absolute permeability, ∇P is the pressure gradient over the core plug and u_g and u_l are the superficial velocities of gas and liquid, respectively (Rognmo *et al.*, 2017).

Foam texture (bubble size) is an important variable affecting the foam viscosity, whereas the finer foam texture has more lamellae per unit length and results in higher resistance to flow. The principal factors affecting foam apparent viscosity in uniform capillaries are dynamic changes at gas/liquid interfaces. These mechanisms are; (1) slugs of liquid between gas bubbles, (2) viscous and capillary forces result in interfaces that are deformed against the restoring force of surface tension, and (3) the surface tension gradient, which is a result of surface-active material being swept from the front of the bubble and accumulated at the back of the bubble (Hirasaki and Lawson, 1985; Friedmann and Jensen, 1986; J. Kim *et al.*, 2005).

CO_2 Foam Mobility Reduction Factor (MRF)

The mobility reduction factor (MRF) characterizes the foam strength. MRF (eq. 2.4) is a dimensionless parameter defined as the ratio of apparent viscosities of foam and no-foam floods at given constant k (Schramm, 1994). Commercial simulators like CMG (STARS and GEM) and ECLIPSE, use the MRF in modeling foam behavior because the foam flooding mechanism is mainly due to increased foam viscosity and reduced gas permeability (Sheng, 2013a).

$$MRF = \frac{\mu_f}{\mu_{nf}} \tag{2.4}$$

where μ_f and μ_{nf} are apparent viscosities of foam and no-foam, respectively.

2.3 Silica Nanoparticle-Stabilized CO_2 Foam Flooding

In recent years, with the development of nano-science, new technologies have provided the alternative of nanoparticle-stabilized CO_2 foam (Yu *et al.*, 2012). Due to their specific characteristics and advantages, the nanoparticles-stabilized emulsion has gained attention compared to foam generated by surfactants (Mo *et al.*, 2012; Sun *et al.*, 2019). Silica nanoparticles are also found to be environmentally friendly due to their natural occurrence in the reservoir. This makes them particularly interesting as EOR agents (Skauge *et al.*, 2010).

The size of nanoparticles (in the range of 1-100 nm) allows unrestricted flow through the small pore throats in most sedimentary rock (Rognmo *et al.*, 2017). Nanoparticles consist of core and surface molecules that are covalently linked or grafted. Electrical and magnetic properties of nanoparticle are mainly controlled by the core, whereas the surface layer of molecules determines the binding affinity for a specific target (Bennetzen and Mogensen, 2014). Nanoparticles are classified into three categories, such as metal oxides, organic, and inorganic (Negin *et al.*, 2016). In EOR applications, spherical silica particles are most commonly used due to their effectivity and low cost (Ogolo *et al.*, 2012). Silica nanoparticles consist of a diameter in the range of several tens of nanometers and the coating extent of silanol groups on their surface control the wettability of the particles (Zhang *et al.*, 2010). The nanoparticle is hydrophilic if over 90% of the surface is covered by silanol groups. They are hydrophobic if only 10% of the particle surface is covered by the silanol groups. Hydrophilic will form a stable oil-in-water emulsion, and hydrophobic will generate emulsions of water-in-oil (Zhang *et al.*, 2010; Ogolo *et al.*, 2012; Negin *et al.*, 2016)

Emulsion is referred to as liquid dispersion in another liquid phase (Berg, 2010). Highly stable emulsions can be generated by using solid nanoparticles. As a foaming agent, silica nanoparticles may stabilize CO_2 foam in the co-injection of CO_2 and nanoparticle solution by creating CO_2-in-water of water-in-CO_2. Nanoparticle emulsions may withstand in the reservoir with high-temperature for an extended period of time (Dicksen *et al.*, 2002; Zhang *et al.*, 2009). Nanoparticles are mechanically and thermally stable, and they are preferred foaming agents in reservoir conditions due to their resistance in high pressure, temperature, shear, and salinity (Bennetzen and Mogensen, 2014). Foam stability is dependent on nanoparticles concentration (Mo *et al.*, 2014). CO_2 foam can be generated with a concentration as low as 100 PPM (Mo *et al.*, 2014).

Retention may cause damage to rock properties like porosity, permeability, and wettability when injecting nanoparticles solution in permeable sedimentary rock. Nanoparticles can be trapped or captured when they move in a formation. This may be caused by three main mechanisms; (i) adsorption of the nanoparticles on the rock surface caused by the Brownian motion, and the electrostatic interaction between the moving particle and the pore wall; (ii) size exclusion, which obtains when the injected particles are more significant than the pore throats; (iii) sedimentation or gravity settling of particles which occurs when there are significant differences between nanoparticles and the dispersed fluid (Gao, 2007). Nanoparticles have lower retention compared to surfactants (Zhang *et al.*, 2009). In sandstone cores, silica nanoparticles show propagation without difficulties (Skauge *et al.*, 2010).

2.4 Surfactant-Stabilized CO_2 Foam Flooding

The main aim of using surfactant (surface-active-agent) flooding is to reduce the interfacial tension (IFT) between oil and water for mobilizing the capillary-trapped residual oil after water flooding (Lake *et al.*, 2014). Surfactants are chemical substances and have an essential role in enhanced and tertiary oil recovery. They adsorb to gas-liquid interface and lowering IFT due to their amphiphilic (hydrophilic and hydrophobic part) molecules. Surfactants can also be used to change wettability, promote emulsification, lower bulk-phase viscosity, and stabilize dispersions (Lake *et al.*, 2014). Co-injection of CO_2 and surfactant solution is able to generate a more stable foam for foam mobility control compared to co-injection of CO_2 and brine solution (Chang and Grigg, 1999).

Surfactants are classified into four major types that are distinguished by the electric charge of the surfactant molecules polar group (Green and Willhite, 1998). These types are; anionic, cationic, nonionic, zwitterionic. Anionic surfactants have been the most widely used in oil recovery due to their ability to reduce the IFT, their stability, their relatively low adsorption on sandstone reservoir rock, and their economic manufacturing process (Zolotukhin and Ursin, 2000). Anionic alpha-olefin sulfonate (AOS) surfactants are used as a foaming agent in many CO_2 foam projects due to their low adsorptions in sandstones (Enick *et al.*, 2012).

In porous media, surfactants are often used to improve foam generation and to stabilize the foam (Enick *et al.*, 2012). Surfactant-stabilized foam relies on continuous regeneration of lamellae in the small pores of the rock for maintaining mobility control. Surfactant types and concentrations have an essential impact on foam texture (bubble size) and viscosity. Increased surfactant concentration leads to smaller bubble size and therefore increase in foam viscosity. Surfactants must satisfy rock surface adsorption, and surfactant solution must fill in the liquid-saturated pore space (Rossen, 1996). In harsh reservoir condition where high temperature, high salinity, surfactants will leave the liquid-gas interface providing short-term stability and more reduced performance (Metin *et al.*, 2011; Mo *et al.*, 2014).

2.5 CO_2 EOR and CO_2 Storage as part of CCUS

Reduction of greenhouse gas (GHG) emissions has been in focus due to global warming and pollution. Therefore, activity on the use of CO_2-driven EOR as well as activity of Carbon Capture Utilization and Sequestration (CCUS) have been increased (Lee and Kam, 2013). Utilization and safe long-term sequestration of CO_2 can be obtained in mature oil fields, which have provided significant interests globally. CO_2 injection for carbon sequestration in deep geological formations is an essential operation for mitigating CO_2 emissions in the atmosphere. CO_2 has to be sequestered in underground formations to limit CO_2 emissions. CO_2 can be stored in the subsurface as (i) mineral precipitates produced by chemical reactions, (ii) dissolved constituent in naturally occurring groundwater, and (iii) free CO_2 in pore spaces of reservoir rock (Pruess *et al.*, 2001; Bachu and Adams, 2003; Leung *et al.*, 2014). Figure 7 illustrates the three main steps for carbon capture and storage (CCS), where firstly CO_2 has to be captured from the fuel source used at power plants and/or industrial facilities, secondly transportation of CO_2 to the storage sites such as depleted oil or gas reservoirs, then thirdly and final step is to inject CO_2 into underground reservoirs for storage.

On the Norwegian Continental Shelf (NCS), the Equinor Sleipner project is considered to be one of the global pioneers of CCS. The project was the first in the world to use pure CCS technology in a deep saline reservoir (Hardisty et al., 2011). CO_2 produced from the Sleipner West Gas Field is separated and injected into the Utsira formation. Since 1996 approximately 1 MMT per year of CO_2 have been separated from the natural gas and stored into a saline aquifer (the Utsira formation) above the hydrocarbon reservoir zones (Steeneveldt et al., 2006).

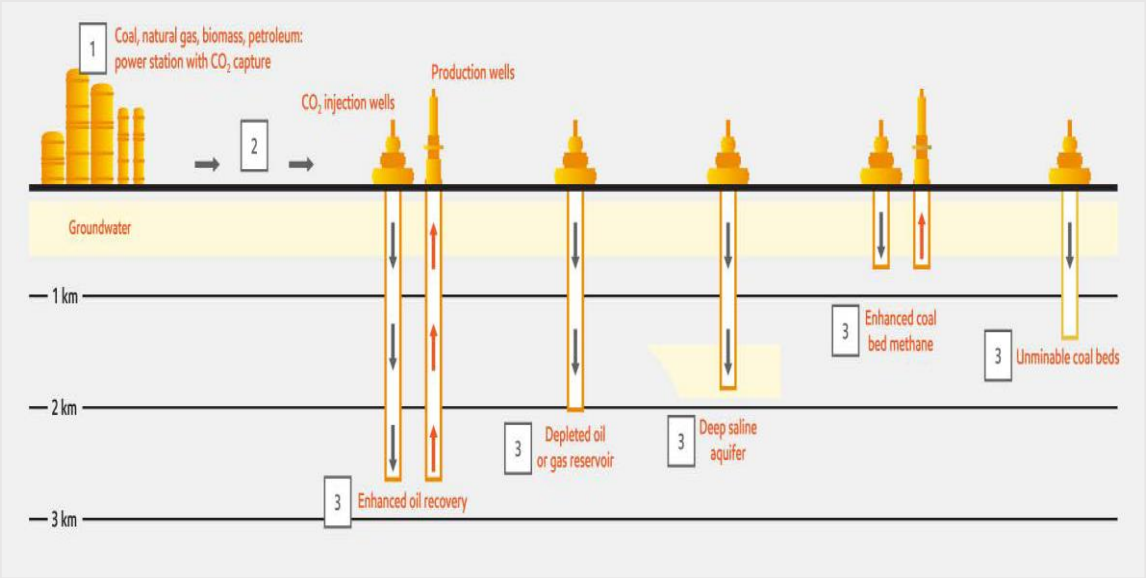

Figure 7: *Carbon capture and sequestration, (1) capturing CO_2 from the fuel source used at power plants or industrial facilities is the first step in the CCS process, (2) transporting the captured CO_2 to the storage sites such as saline aquifers and depleted oil or gas reservoirs, and (3) injecting CO_2 into underground reservoirs for storage. Adapted from (Exxon Mobil, 2019).*

2.6 Reservoir Simulation

In the oil industry, reservoir simulation is considered the standard for solving reservoir engineering problems. Reservoir simulation refers to the construction and operation of a model whose behavior assumes that of actual reservoir behavior (Abou-Kassem *et al.*, 2013). In oil recovery, reservoir simulation estimates the field performance under one or several producing schemes. In simulators, the reservoir is divided into three dimensions in discrete units. In a series of discrete steps, fluid properties and reservoir's development are modeled through space and time. It is essential to define model geometry, rock, and fluid properties, and initial fluid distribution for each cell in order to make the simulation model as realistic as possible. These can be obtained from well-logs, geological and geophysical analysis, and experimental studies on core plugs (Computer Modelling Group Ltd, 2016).

2.6.1 Numerical Modelling in CMG™

Computer Modelling Group (CMG™) provides three modeling simulator tools (Computer Modelling Group Ltd, 2017). These tools are IMEX (**IM**plicit-**EX**plicit Black Oil Simulator), GEM (**G**eneralized **E**quation of State **M**odel Reservoir Simulator) and STARS (**S**team, **T**hermal, and **A**dvanced Process **R**eservoir **S**imulator). In this thesis, the numerical models created and investigated are simulated with GEM simulator. According to Computer Modelling Group LTD (2017), CMG-GEM can be described as the following; CMG-GEM is advanced Equation-of-State (EOS) compositional reservoir simulator (Computer Modelling Group Ltd, 2016). The unconventional simulator is used to study the complex compositional and inter-phase interactions of multiphase reservoir fluids during primary and enhanced recovery operations. It is used extensively for CO_2-processes. Phenomena such as viscosity and IFT variation, vaporizing and swelling of oil, liquid drop out from gas, in addition to miscibility between two fluids can be investigated through GEM. GEM allows cartesian, cylindrical, and variable thickness grids, as well as explicit, thoroughly, and adaptive implicit solution models (Computer Modelling Group Ltd, 2017).

In GEM, the Peng-Robinson equation of state is used to perform the phase change calculations. The Equation-of-state (EOS) establishes a relationship between pressure, molar volume, and temperature data to calculate the phase behavior (Computer Modelling Group Ltd, 2016). CMG's WinProp program is an Equation-of-State (EOS)-based fluid behavior and PVT (pressure-volume-temperature) modeling. In WinProp laboratory data for fluids can be imported, and an EOS can be tuned to match its physical behavior (Computer Modelling Group Ltd, 2017). Fluid interactions can then be predicted, and a fluid model may be created for use in CMG-GEM. GEM has seven different keywords groups. These sections need to be followed in every simulation deck file (Computer Modelling Group Ltd, 2017):

- Input-Output control
- Reservoir description
- Component properties
- Rock Fluid data
- Initial conditions
- Numerical method control
- Geo-mechanics Data
- Well and recurrent data

In a compositional model, the equilibrium flash calculations by EOS has to be used to determine hydrocarbon phase compositions where the mass balance are made for each hydrocarbon component (Computer Modelling Group Ltd, 2016). CMG-GEM is used to model core flooding experiments in this thesis, injecting CO_2-brine, together with and without nanoparticles as the foaming agent.

2.6.2 History matching

History matching is a forward modeling technique that involves adjusting a reservoir/core model in a numerical reservoir simulator until it reasonably models the historical behavior of an existing reservoir and wells. History matching is a classical mathematical problem where the closer the initial guess is to the correct answer, the faster the convergence is to the correct answer (Baker *et al.*, 2006). It is necessary to history match measured performance, such as pressure distribution and fluid productions in order to validate a reservoir model (Mattax and Dalton, 1990; Archer and Wall, 2012). The intention of history matching is to find the reservoir parameters that can minimize the difference between the model performance and the historical performance of the field. History matching reduces the reservoir model uncertainties (Fanchi, 2005).

There are three general components of a history match; (1) historical match of rates and cumulative volumes, (2) history match recent data, and (3) history matching infill well results (Baker *et al.*, 2006). After a successful history match, the model can be used for further predictions of future reservoir behavior and production. It is essential to have a better understanding of how reservoir properties vary in the reservoir to achieve correct predictions of reservoir performance in the future. History match parameters are controlled by physical parameters, such as relative permeability, permeability distribution, and porosity (Baker *et al.*, 2006).

In this study, CO_2 relative permeability was investigated for different injection rates in order to obtain a history match of experimental observations, including differential pressure and foam apparent viscosity. Upon achieving the history match, a sensitivity analysis was conducted by changing some of the foam model parameters during CO_2 foam flooding.

2.7 Overview of Two-Phase Relative Permeability

The two-phase relative permeability is one of the most important parameters to consider when simulating the flow of water/gas and water/oil systems. Relative permeability is the ratio of the effective permeability and absolute permeability, and it is a key parameter in modeling multiphase flow scenarios. Relative permeability depends strongly upon wettability, as wettability is a property with a significant impact on fluid saturation and distribution. Lately, the growing research interests in CO_2 geological storage have motivated both experimental measurements of CO_2-brine relative permeabilities (Bennion and Bachu, 2010; Mosavat *et al.*, 2014) and modeling studies on CO_2 geological storage that use CO_2 relative permeability as a key input (Doughty, 2005; Kamali *et al.*, 2015).

Corey developed the power-law model to describe the relative permeability as a function of normalized gas saturation (Corey, 1954). The Corey-type relative permeability functions to be applied in the CO_2/water have the following forms (see Eq. 2.5 – Eq. 2.7).

$$k_{rg} = k_{rg}^{0} \, (S_g^*)^{n_g} \tag{2.5}$$

$$k_{rw} = k_{rw}^{0} \, (1 - S_g^*)^{n_w} \tag{2.6}$$

$$S_g^* = \frac{S_g - S_{gi}}{1 - S_{gi} - S_{wr}} \tag{2.7}$$

where k_{rg} and k_{rw} are relative permeability to gas and water respectively , k_{rg}^{0} and k_{rw}^{0} are maximum relative permeability of gas and water respectively, S_g^* is the normalized gas saturation which is a function of gas and residual water saturation, n_g and n_w are Corey exponents for gas and water respectively, S_g and S_{gi} are gas and initial gas saturation respectively and S_{wr} is the irreducible water saturation. In this study, the exponents n_g and n_w range from 1 to 3. The maximum relative permeability values, k_{rg}^{0} and k_{rw}^{0} are between 0 and 1.

Corey functions also calculate the relative permeability in water/oil as a function of normalized water saturation. The following equations (Eq. 2.8 – Eq. 2.10) are used based on the work presented by (Corey, 1954):

$$k_{rw} = k_{rw}^{0} \, (S_w^*)^{n_w} \tag{2.8}$$

$$k_{ro} = k_{r0}^{0} \, (1 - S_w^*)^{no} \tag{2.9}$$

$$S_w^* = \frac{S_w - S_{wi}}{1 - S_{wi} - S_{or}} \tag{2.10}$$

where k_{rw} and k_{ro} are relative permeability of water and oil respectively , k_{ro}^{0} and k_{rw}^{0} are maximum relative permeability of oil and water respectively, S_w^* is the normalized water saturation which is a function of water and residual oil saturation, n_o and n_w are Corey exponent for oil and water respectively, S_w and S_{wi} are gas and initial water saturation respectively and S_{or} is the residual oil

saturation. In this study, the exponents n_o and n_w range from 2 to 4. The maximum relative permeability values, k_{ro}^0 and k_{rw}^0 are between 0 and 1. The relative permeability curves used in this work were established by using the empirical relative permeability correlations of the above modified Corey.

Chapter 3: Methods

This chapter describes the data acquisition procedure for obtaining experimental data and deriving the model input data. A brief description of the experimental procedure, performed by Rognmo and other members of the Reservoir Physics Group, is outlined. Please refer to Rognmo et al. (Rognmo *et al.*, 2017) for further details about the performed experiment. This chapter also describes the simulation set up and outlines the proposed methodology for the determination of model input parameters, including residual water saturation, water-gas end-point relative permeability, and Corey exponents. Additionally, the selection and tuning of parameters to history match the quality scan are discussed.

3.1 Review of Foam Quality Scan Experiment

Experimental work at the Reservoir Physics Group is used as the basis for the simulation work in this thesis. Core flooding was performed on a homogeneous Bentheimer sandstone outcrop core, denoted ST3. Bentheimer consists of quartz (95%), feldspar (< 2%) and clays (3%) (Rognmo et al., 2017). The summary of rock and fluid properties is shown in Table 3.1.

Table 3. 1: *Summary of Rock and Fluid properties for core ST3 (Rognmo et al., 2017).*

Core diameter, D [cm]	3.77
Core length, L [cm]	28.8
Porosity ∅, [%]	23.8
Permeability, κ [mD]	2252
Pore volume, V_p [cm^3]	76.5
Brine viscosity, μ_{brine} [cP]	1.03
CO_2 viscosity, μ_{CO2} [cP]	0.079^a
Initial brine saturation, S_{wi}	1
Initial CO_2 saturation, S_{gi}	0
Experimental conditions	20 °C / 9000 kPa
Nanoparticle concentration [ppm]	1500^b
Brine density ρ_{brine} [g/cm^3]	1.01
Nanofluid density ρ_{NP} [g/cm^3]	1.01
CO_2 density ρ_{CO2} [g/cm^3]	0.843^a

a Value obtained from National Institute of Standards and Technology Database NIST (2017).

b The nanoparticle (Colloidal silica) concentration in the aqueous solution at 0.15 wt% (equivalent to 1500 ppm by mass) (Rognmo et al., 2017).

Nanoparticle-stabilized CO_2-foam was investigated during co-injections of nanofluid and liquid CO_2 at different gas fractions and total volumetric flow rates. The following injection strategy was used to evaluate foam strength and stability: co-injection with a monotonically increasing gas fraction from 0.1 to 1.0, referred to as drainage-like flow sequence. The total volumetric injection rates were 120, 180, and 240 mL/h. Only surface-modified nanoparticles were used as a foaming agent to generate foam *in situ* (i.e., no surfactant). For the drainage-like flow sequence, the following procedure was followed: (i) start with the lowest injection rate at the lowest gas fraction (f_g = 0.1) and co-inject nanofluid (NP) and CO_2 until the pressure stabilizes, (ii) increase injection rate monotonically, at the same f_g, and establish stable differential pressure, (iii) change the injected gas fraction to the next gas fraction (f_g = 0.2) and repeat step (i) and (ii). Near-Newtonian CO_2 foam defined as constant apparent viscosity was observed with changes in injection rates at each gas fraction during the co-injection of nanofluid and CO_2 (Rognmo et al., 2017). Co-injection with liquid CO_2 and nanofluid were benchmarked against baseline co-injections performed without a foaming agent (see Figure 8) in similar rock samples with identical experimental conditions. This was to evaluate foam strength and degree of CO_2 mobility reduction.

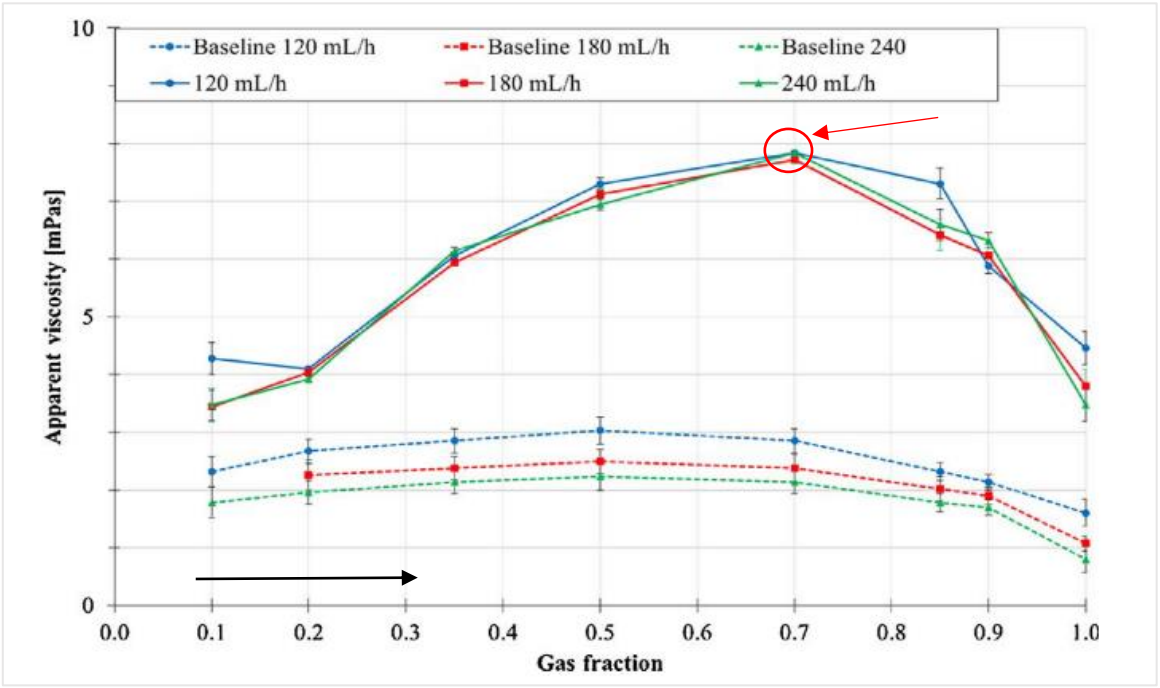

Figure 8: *Apparent viscosity versus gas fraction for both baseline and foam co-injections. Co-injection of CO_2 and nanofluid (solid lines). Three constant total injection rates were used (rates are indicated with similar colors: 120 mL/h blue; 180 mL/h red; 240 mL/h green) with gas fraction varied between f_g = 0.1 and 1.0. Co-injections with nanoparticles were benchmarked against baseline co-injections with brine and CO_2 (dashed lines). The lines between points are only to guide the reader and not measured (Rognmo et al., 2017). The red arrow and circle represent the maximum apparent viscosity achieved by CO_2-NP co-injections. The black arrow points the way the injections were performed with regard to the injected gas fractions.*

In co-injection of CO_2 and NP, it was observed that the apparent viscosity increased to a maximum value (7.8 cP) at f_g = 0.7, indicates the optimal gas fraction and transition for the low-quality regime(f_g <0.7) to the high-quality regime (f_g >0.7). For the baseline co-injections (without nanoparticles), the apparent viscosity was almost 3 times lower compared with NP co-injections at the same gas fraction (f_g = 0.7). Figure 8 showed these experimental results.

3.2 Core Flood Simulation in CMG/GEM

3.2.1 Static Model Set-up

The simulation set-up consists of a one-dimensional linear model with the direction of flow in the I-direction (Figure 9). The cross-sectional area (A) of the simulation model, $A = DJ * DK$, is equal to the core used in the experiment discussed above. The linear simulation model is divided into 50 individual grid cells in the flow direction (I-direction) (Computer Modelling Group Ltd, 2017).

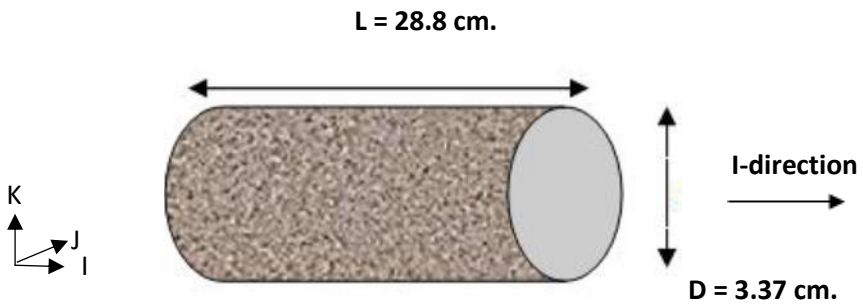

Figure 9: *Diagram of the laboratory core sample, modified from (Computer Modelling Group Ltd, 2016).*

A Cartesian grid was built of the static core system using the above-described dimensions using the commercial CMG™ builder (Figure 10). The dimension of the core model was 50 x 1 x 1, in i-, j- and k-directions, respectively, as seen in Figure 10. A sensitivity study on 50, 100, and 1000 grid cells was first conducted in order to choose the optimal number of grid blocks to accurately capture foam behavior without hindering simulator performance. It was found that the most appropriate number of grid blocks was 50, in order to avoid numerical dispersion. This number was found by constructing a black oil model with a core of the exact dimensions and comparing oil recovery with different grid block sizes. The model has individual grid cell dimensions of 0.576 cm in length, 3.34 cm in width and 3.34 cm in thickness. The simulation model is oriented horizontally, just like the experiment was performed. Table 3.2 shows the core model properties.

Table 3. 2: *Core model properties.*

Number of grid blocks (i, j, k)	$50 \times 1 \times 1$
Grid block size	$0.576 \times 3.34 \times 3.34\ [cm^3]$
Porosity Ø	0.238
Permeability $k_x = k_y = k_z$	2252 [mD]
Initial temperature	20 $[°C]$
Initial pressure	9000 [kPa]
Initial water saturation	1

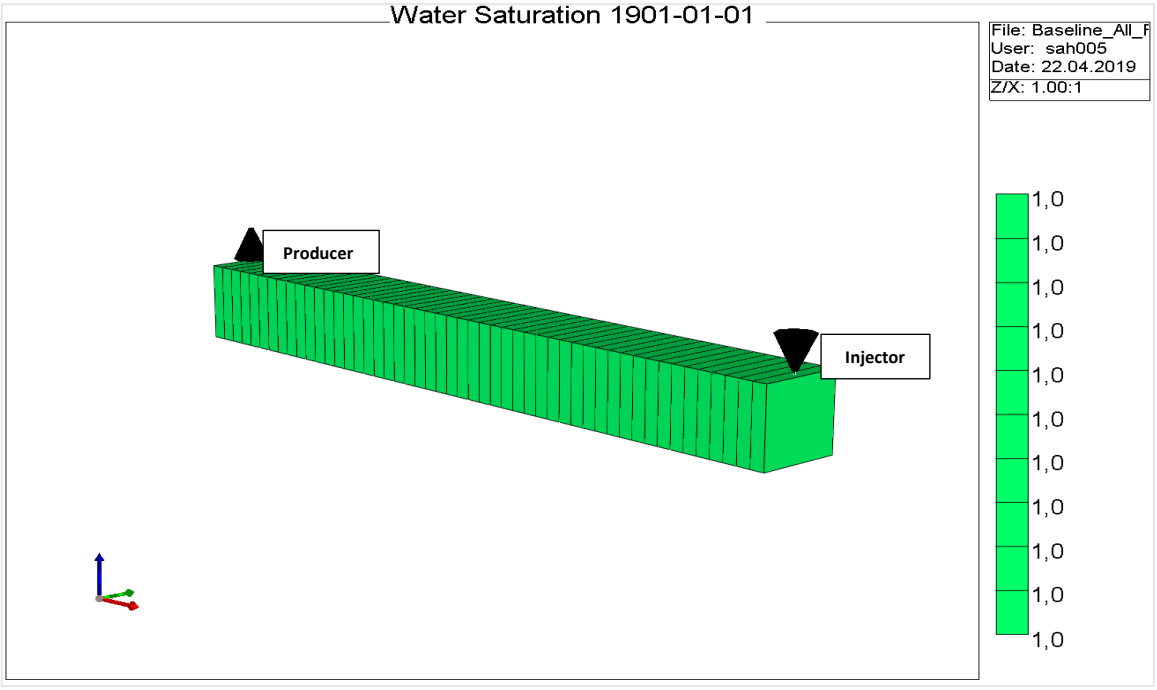

Figure 10: *3-D view of the constructed model.*

3.2.2 Dynamic Model Set-up

Core dimensions and initial conditions of the experiment, such as temperature, pressure, and water and gas saturation, were used as inputs in the simulation. Additionally, rock properties, permeability, porosity, gas, and water viscosity were also used as inputs. Total volumetric injection rates for both liquid and gas and foaming agent concentrations were also used as inputs for the simulation work. Some of these properties, including parameters used to estimate water-oil relative permeability curves, were constant for all of the performed simulations, as shown in Table 3.1. Core and fluid properties were kept identical to the experimental system (Table 3.1). No data was available for the relative permeability curves for core ST3. The initial relative permeability curves were, therefore derived from estimated data, using the residual water saturation, end-point CO_2 relative permeability and Corey exponents for water and gas. The connate water saturation was determined from the literature. The estimated data of the water-oil and gas-water relative permeability curves in the base model (the base CO_2-brine model) were obtained from history matching of the baseline flood (co-injection of CO_2 and brine). The relative permeability curves were obtained from the modified Brooks-Corey equations discussed in Chapter 2.7. Two sets of relative permeability curves were used, which are referred to as water-oil (Set-1) and CO_2-water (Set-2). Relative permeability Set-1 and Set-2 properties are discussed in Chapter 4.1. Because the relative permeability curves were unknown, this approach was used for the initial set of water-oil and gas-water relative permeability curves; they were considered the most uncertain parameters to be tuned in the first phase of history matching.

3.2.3 Modeling Foam

A commercial foam model was used to represent nanoparticle-stabilized CO_2 foam. CMG/GEM empirical foam model is typically used for the modeling of the CO_2 foam process using surfactant as a foaming agent, but for this work, nanoparticle was used. The simulator is based on local steady-state (or local equilibrium) modeling where a predetermined value for the gas-phase mobility reduction factor (FMMOB) must be used as an input. The presence of foam affects the viscosity and relative permeability of the gas phase significantly, but not those of the liquid phase (Friedmann et al., 1991). CO_2 mobility is scaled down by inverse mobility reduction factor FM, which is equivalent to modeling the apparent viscosity of the foam, as shown in equation 3.1. The subscript *f* refers to foam.

$$k_{rg}^{f} = k_{rg} \times FM \tag{3.1}$$

where k_{rg}^{f} is the foam relative permeability, k_{rg} is the gas relative permeability and FM is the mobility reduction factor.

The FM factor involves seven functions that describe the factors that influence CO_2 mobility reduction, including water saturation, oil saturation, surfactant concentration, and capillary effects, as shown in equation 3.2. The range of FM is between 0 and 1. FM = 0 is related to the strongest foam allowing no gas to flow, and FM = 1 means no foam (Computer Modelling Group Ltd, 2017).

$$FM = \frac{1}{1 + FMMOB(F1 \times F2 \times F3 \times F4 \times F5 \times F6 \times F7 \times FDRY)} \tag{3.2}$$

The FMMOB parameter represents the maximum mobility reduction factor or the reference mobility factor, capillary number (flow rate), zero oil saturation, S_o = 0, and oil mole fraction of component (Computer Modelling Group Ltd, 2017). The remaining parameters represent the effect of foaming agent concentration ($F1$), the detrimental effect of oil ($F2$), the flow velocity for both shear thinning ($F3$) and generation effects ($F4$), the oil composition($F5$), the effect of salinity ($F6$), the permeability dependence parameters ($F7$) and the foam dry-out effect (FDRY) (Computer Modelling Group Ltd, 2017). The F functions ($F1, \ldots . F7$) are ranging from 0 to 1. FDRY is defined in the CMG/GEM model as:

$$FDRY = 0.5 + \frac{\arctan(Sfbet(S_w - Sfdry))}{\pi} \tag{3.3}$$

In the dry-out function in equation 3.3, the parameter Sfbet controls the sharpness of the transition foam from a high-quality regime to a low-quality regime (dry-out slope). Sfbet with a very high value represents a sharp transition and foam collapse within a narrow range of saturation whereas a low value of Sfbet represents a foam collapse that is not abrupt (Farajzadeh et al., 2015). The parameter Sfdry is the water saturation at which foam experiences significant coalescence (maximum dry-out value) (Computer Modelling Group Ltd, 2017). During history matching, the main focus is on the effect of FMMOB and the dry-out (FDRY) function due to the availability of the experimental data. Choosing the value of the foam parameter FMMOB was a challenge since CO_2/nanoparticles foams may generate

weak foams compared to CO_2/surfactant foams, therefore lower values of FMMOB should be used. The range of FMMOB and the dry-out function (Sfdry+Sfbet) that were estimated is presented in Chapter 4.2.2 , while F functions have been defaulted to 1. A full description of the dependent F functions can be found in Table A.1 in Appendix A.1.

3.2.4 History Matching Workflow

In this work, a history matching strategy is used for tuning model parameters using experimental observations and results collected through a series of simulations. The aim was to validate the model and reduce uncertainty by reproducing experimental observations. The experimental metrics matched were differential pressure and apparent viscosity. Differential pressure and apparent viscosity were chosen to be matched because they were the only available results from the experimental data done by Rognmo et al. (Rognmo et al., 2017). The first phase of the history match focused on tuning the initial relative permeability curves to reproduce experimental observations from a baseline (without nanoparticles) foam quality scan. The second phase of the history match used relative permeability curves from Phase 1 and emphasized tuning the foam model parameters and their impacts on injection and production pressure. Foam generation during co-injections of CO_2 and nanofluid (NP) was observed at variable gas fractional flow.

Phase 1 History Matching

Phase 1 includes history matching the baseline CO_2-brine foam quality scan (without nanoparticles) by tuning relative permeability curves. The set of parameters used to establish relative permeability curves, shown in Table 3.3, are categorized into groups according to the part of the model in which they contribute. These include; water-oil relative permeability, CO_2 relative permeability, and foam model parameters. Parameters that are known through the experiments are the initial gas saturation (S_{gi}) and the relative permeability of water at the initial gas saturation (S_{wr}). The end-point CO_2 relative permeability (k_{rg}^0) was evaluated through a series of history match runs using the Corey model. The rest were determined through a series of simulations, by matching the baseline (CO_2-brine co-injection at residual water saturation), where Corey curvature of the gas (n_g) and end-point gas relative permeability (Table 3.3).

The objective of performing a baseline match is to tune the parameters of CO_2 relative permeability, by determining the Corey curvature of the gas and the gas relative permeability curves. The relative permeability properties for water-oil (Set-1) and gas-water (Set-2) are presented in Chapter 4.1, where water-oil relative permeability curves were not changed because the oil was not included in the experiment work. The water-oil relative permeability table must be included in order to run the model in CMG. By tuning the gas-water relative permeability curves in the simulation model, the best match of differential pressure and apparent viscosity was achieved. Firstly, an initial estimation of Corey parameters was made based on experimental values. In order to make an initial estimation, end-point relative permeabilities of water, oil and gas had to be calculated from the available experimental data. The baseline co-injections were then fitted to obtain the gas relative permeability parameters (n_g, k_{rg}^0, S_{gi}).

Table 3. 3: *The set of all the parameters used for the simulation of the CO_2 foam process.*

Water-oil Relative Permeability	CO_2 Relative Permeability	Foam Model Parameters
n_w	n_w	FMMOB
n_o	n_g	Sfdry
k_{rw}^0	k_{rwsgi}^0	Sfbet
k_{ro}^0	k_{rg}^0	
S_{or}	S_{wr}	
S_{wr}	S_{gi}	

Phase 2 History Matching Foam Model Parameters

After tuning the relative permeability curves in Phase 1, foam model parameters (Table 3.3) are tuned in order to give the best match to the experimental data during the foam quality scan with nanoparticles. Initial foam model parameters were derived from the default values in CMG. Foam quality tests (CO_2-NP co-injection at residual water saturation), were then fitted to obtain the reference foam mobility reduction factor, FMMOB, the foam dry-out function, which is modeled by Sfbet and Sfdry. A history match is performed, where these parameters (FMMOB, Sfbet, and Sfdry) are determined, and the limitations of the model to simulate the experimental performance of CO_2 co-injections processes are discussed. For the rest of the parameters, a sensitivity study is performed, to examine the significance of the parameters on the apparent viscosity and the differential pressure.

3.2.5 Sensitivity Analysis

Several sensitivity studies were performed to understand how uncertain model parameters impact the simulation results, including differential pressure and foam apparent viscosity. This was to demonstrate the model's ability to represent the complex foam processes, and it was also the necessary background to give a better understanding of how to match the laboratory-measured results from the core floods described in Chapter 3.1. This sensitivity study used the co-injection of nanofluid and CO_2 as a foam reference case, where the total injection rate is 240 mL/h with increasing gas fractions (f_g = 0.1 to 1.0). By changing one parameter at a time, each parameter was analyzed independently. Benefits of this systematic change are; simple to use, easy to understand the results, and the results are not complicated by the effects of other parameters. The following parameters were investigated through a series of simulations presented in Chapter 4.3.

- **Nanoparticle concentration:** Model sensitivity to nanoparticle concentration in the aqueous solution was varied between 0.02 and 1.0 wt%, where a concentration of 0.15 wt% was used as a reference in the foam reference case. The purpose of this investigation is to see how different concentrations impact the differential pressure. According to Khajehpour et al. (2016), different concentrations showed significant increases in the amount of foam generation and stabilization (Khajehpour *et al.*, 2016).

- **FMMOB:** Model sensitivity to the reference foam mobility reduction factor was conducted, which is used in the dimensionless foam interpolation calculation. FMMOB allowed range is 0 to 10^5 in CMG. However, in this work, low values were chosen since the foaming agent is nanoparticle, rather than surfactant. In the case of surfactants, higher values of FMMOB must be used since surfactants generally generate stronger foam (higher apparent viscosity). By

using different values of FMMOB, it can be seen that the apparent viscosity changes with changing the mobility reduction factor. FMMOB values of 3, 6.7, 10 and 20 were used in this sensitivity study.

- **Sfdry:** Model sensitivity to the maximum dry-out value was conducted, which used in the dimensionless foam dry-out calculation. Sfdry is the water saturation at which foam experiences significant coalescence. The allowed range of Sfdry is 0 to 1.0. For the sensitivity study values of 0.3, 0.5, and 0.6 were used.

- **Sfbet:** Model sensitivity to the reference dry-out slope was conducted, which used in dimensionless foam dry-out calculation. Sfbet controls the sharpness of the transition of foam from a high-quality regime to a low-quality regime. Sfbet allowed range is 0 to 10^5 in CMG. Three different values of Sfbet were used in the sensitivity, 10, 100 and 1000.

- **Absolute permeability (K):** Model sensitivity to absolute permeability was conducted to analyze its impacts of foam apparent viscosity. Absolute permeability is defined as the capability of the porous media to transmit a single fluid through its network of interconnected pores (Zolotukhin and Ursin, 2000). For the foam reference case, the absolute permeability value was 2252 mD. This value considered as a high value according to literature. Two more values (i.e., 1000 and 500 mD) were investigated in order to see their impact on the apparent foam viscosity.

- **Total injection rate (Q_T):** Model sensitivity to total injection rate (injection velocity) was conducted, which used in mL/h or m^3/day (simulation input unit). The injection rates from 120 mL/h to 500 mL/h were used in the sensitivity analysis. The foam apparent viscosity was investigated for the different injection rates. The foam rate scan was conducted to study the rheology of foam at different injection rates where the CO_2 and nanofluid co-injections were performed at constant gas fractions of 0.7 and 0.8.

Chapter 4: Results and Discussion

4.1 Phase 1 – Relative Permeability

Tables 4.1 and 4.2 show an overview of the values used in constructing the relative permeability curves for oil-water (Set-1) and water-gas (Set-2), respectively. Parameters in Table 4.1 and 4.2 were calculated using equations listed in Chapter 2.7. The capillary end effect was assumed to be zero for both tables. Water end-point relative permeability is assumed to be 1 since the outcrop core (ST3) was initially 100 % saturated with brine, while the rest of the parameters were estimated, as shown in Table 4.1 and 4.2. Figure 11 shows the water-oil relative permeability curves. As mentioned earlier, the water-oil relative permeability table must be included in order to run the model.

Table 4. 1: *Experimental and estimated values of relative permeability parameters of Set-1.*

Parameter	Experimental Value	Estimated Value
Residual water saturation, S_{wr}	-	0.2
Residual oil saturation, S_{or}	-	0
Water end-point relative permeability, K_{rw}°	1	1
Oil relative permeability @ S_{wr} , K_{ro}°	-	1
n_w	-	4
n_o	-	2

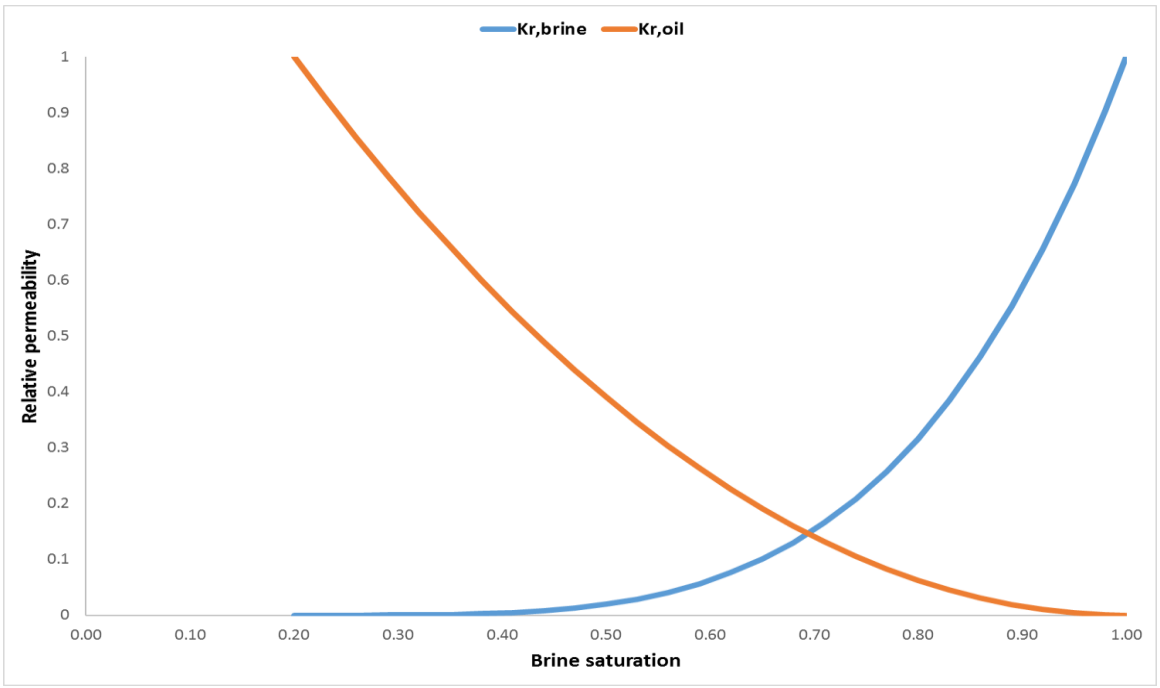

Figure 11: *Relative permeability curves of brine and oil as a function of brine saturation, calculated from Set-1 parameters listed in Table 4.1. The blue line is the water relative permeability curve (Kr, brine), while the orange line is the relative permeability curve for oil (Kr, oil).*

Relative permeability curve estimation was performed in order to determine the gas end-point relative permeability. Different sets of gas relative permeability were defined up to a gas saturation of 0.8, as shown in Figure 12, and their effect on pressure drop was examined. Figure 12 shows the variation of CO_2 end-point, where the best match to the CO_2-brine baseline foam quality scan is 0.13 (red curve). A total of seven simulation runs were performed to fit the experimental differential pressure of the baseline (CO_2-brine), where six of them were not able to match the experimental differential pressure data. Figure 13 shows the differential pressure percentage difference from the history match, which was obtained through a series of simulations on different gas relative permeability end-points. The injection rate of 120 mL/h was used. It was observed that the minimum percentage difference (black columns) obtained was with gas relative permeability end-point of 0.13. At this end-point value, the differential pressure from the simulation was in good agreement with the experimental data. Therefore, a gas relative permeability end-point of 0.13 was used in further investigations to find the slope of the gas relative permeability curves, which can be used as input for the model.

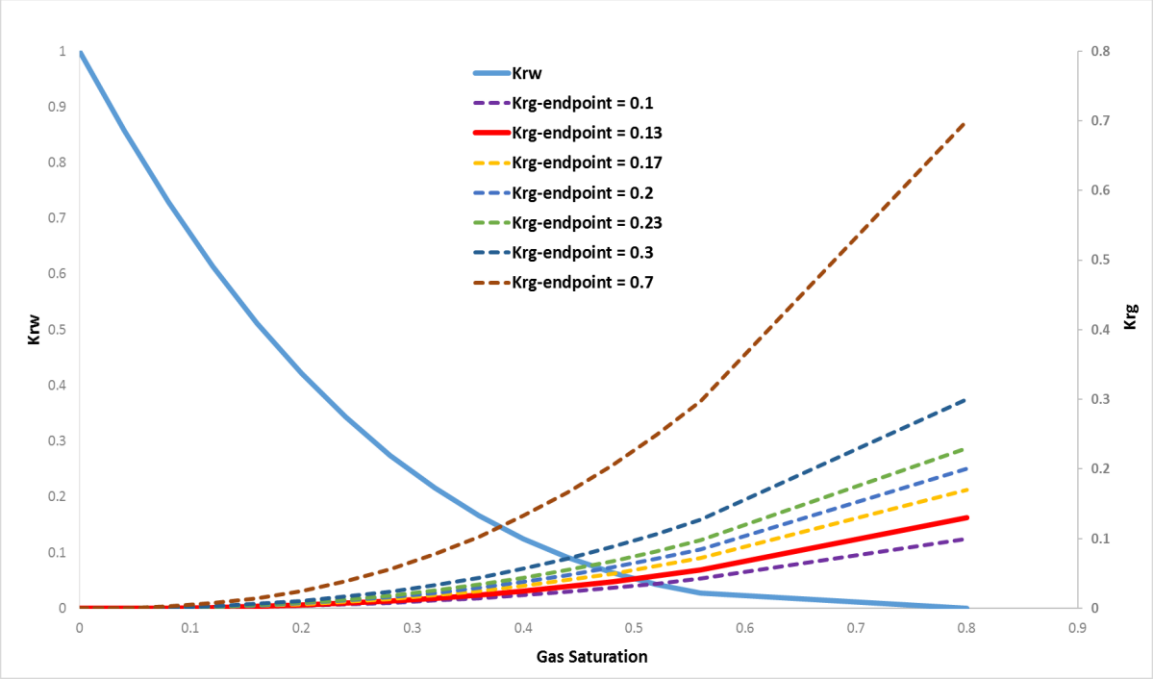

***Figure 12**: Comparison of CO_2-brine relative permeability curves for different CO_2 end-point relative permeability for the injection rate of 120 mL/h. The solid red line is the best match gas relative permeability curve, while the solid blue line is the water relative permeability curve.*

***Figure 13**: Comparison of differential pressure percentage difference from the baseline CO_2-brine experiment for CO_2 end-point relative permeability. The injection rate was 120 mL/h. The black columns presented the differential pressure percentage difference when the gas end-point is 0.13, which gives the best match for the experimental data.*

The parameter values for Set-2 are shown in Table 4.2 below:

***Table 4. 2:** Experimental, initial estimated, and best match values for relative permeability parameters of Set-2.*

Parameter	Experimental Value	Initial Estimated Value	Best Match Value
Residual water saturation, S_{wr}	-	0.2	0.2
Initial gas saturation, S_{gi}	0	0	0
CO_2 end-point relative permeability, K°_{rg}	-	0.7 – 0.1	0.13
Water relative permeability @ S_{gi} , K°_{rwsgi}	1	1	1
n_w	-	3	3
n_g	-	4	1.8 - 2.4

In order to create an estimation of gas relative permeability curves, Corey curvature for the gas was varied between 1.8 and 2.4 for each injection rate, as shown in Table 4.2. Figure 14 shows gas-brine relative permeability curves, where increasing n_g from 1.8 to 2.4 implies a general reduction in gas relative permeability away from end-point value. The decrease in gas relative permeability (k_{rg}) results in higher differential pressure. Relative permeability curves are shown in Figure 11 and Figure 14 were used for the simulation runs in both baseline foam quality scans and foam quality scans with nanoparticles present.

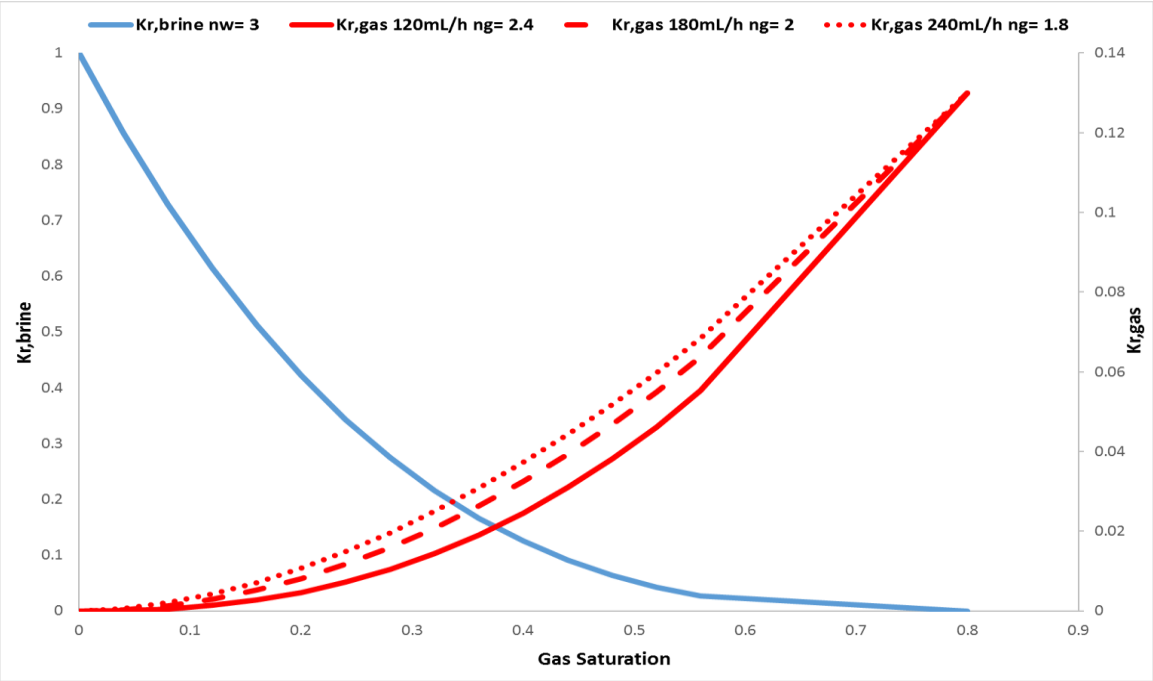

Figure 14: *Relative permeability curves of CO_2 and brine (without nanoparticles) as a function of gas saturation, calculated with parameters Set-2 listed in Table 4.2. The blue line is the water relative permeability curve, the solid red line is the gas relative permeability curve for the injection rate of 120 mL/h, while the red square dotted line and red round dotted line are the gas relative permeability curves for the injection rates 180 mL/h and 240 mL/h, respectively. The Corey curvatures for the gas were 1.8, 2 and 2.4 for the injection rates of 240, 180 and 120 mL/h, respectively.*

4.2 History Matching

This section presents the history matching study to model the experimental core floods performed on the Bentheimer outcrop core (ST3). It focuses on the model input/output and interpretation of the results. Relative permeability parameters obtained for history matching are listed in Table 4.1 and 4.2 in Chapter 4.1. Manual history matching was performed to tune the most uncertain model parameters to get the best match between simulation results and experimental data. The variables which have been changed for manual history matching were end-point gas relative permeability (K_{rg}°), Corey curvature for gas (n_g), reference foam mobility reduction factor (FMMOB), and maximum dry-out parameter (Sfdry).

4.2.1 History Matching the Baseline CO_2-brine Foam Quality Scan

Baseline Differential Pressure – History Match

Figure 15 shows the differential pressure history matching results of the foam quality baseline (CO_2-brine coinjection) for the total injection rates of 120, 180, and 240 mL/h. In Figure 15, solid lines are the history match differential pressure curves, and the points are the experimental differential pressure data. A total of 2 PV were injected for each gas fraction in order to achieve a steady-state with the injection rate of 120 mL/h, while 1.5 pore volume (PV) was injected at rates of 180 mL/h and 240 mL/h. Injection rates are indicated with similar colors (120 mL/h red; 180 mL/h orange; 240 mL/h blue). The baseline co-injection started from f_g = 0.1 and increased to f_g = 1.0 for the injection rates of 120 mL/h and 240 mL/h, and from f_g = 0.2 to f_g = 1.0 for the injection rate of 180 mL/h. An increase of 10 % in differential pressure for all rates was observed with increasing gas fraction until it reached f_g = 0.5. At this gas fraction, the highest differential pressures dP = 11.72, 14.23, and 16.97 kPa were achieved for total injection rates of 120, 180, and 240 mL/h, respectively. For f_g >0.5, brine injected volume was lower than CO_2 injected volume. CO_2 flows easily in the larger pores, resulting in the more continuous gas phase and higher gas relative permeability, while brine flows in the small pores and along pore-walls, and hence, differential pressure decreases slightly. In a water-wet system, water occupies the smallest pores, while in the larger pores, gas trapping occurs (Ettinger and Radke, 1992; Dicksen et al., 2002). The history match results and the experimental differential pressure data were in good agreement, as shown in Figure 15. Table A.2.1 in Appendix A.2 also shows the experimental and simulation results for differential pressure.

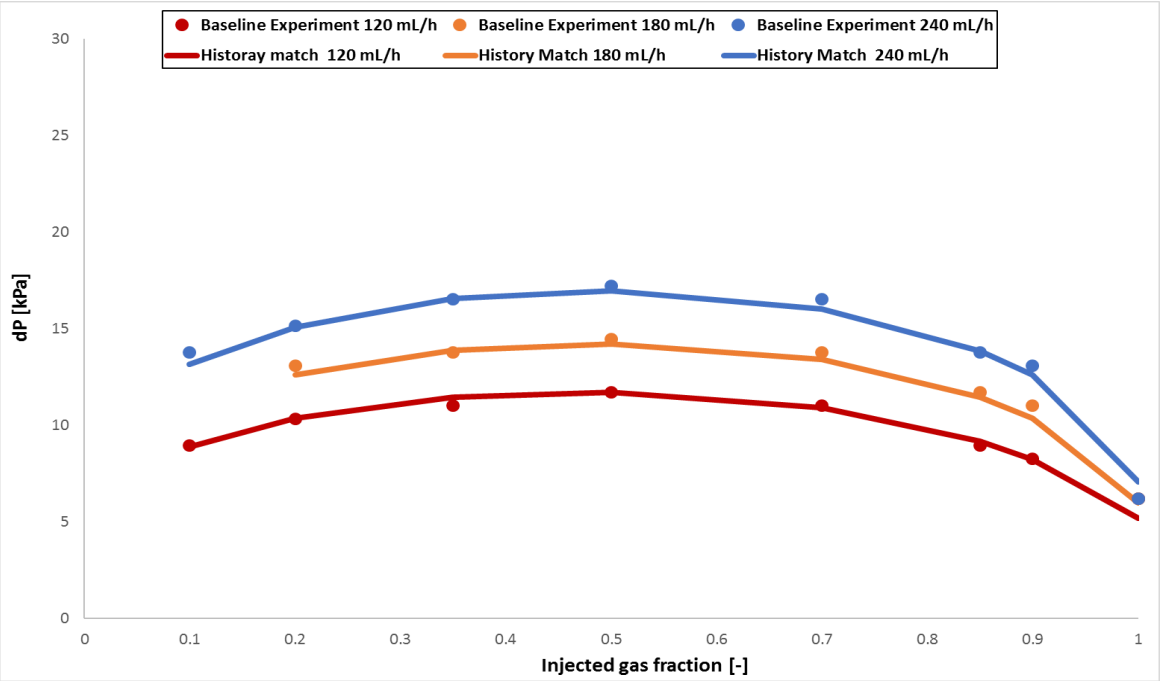

Figure 15: *History match of the baseline steady-state average differential pressure versus gas fraction during the coinjection of CO_2 and brine. Experimental data (points) and history match data (solid lines). Three constant total injection rates are used (rates are indicated with similar colors: 120 mL/h red; 180 mL/h orange; 240 mL/h blue) with the gas fraction varied between f_g = 0.1 and 1.0. The maximum differential pressure is observed at f_g = 0.5 in all the three injection rates.*

Baseline Apparent Viscosity - History Match

Figure 16 shows the apparent viscosity of the experimental baseline data and simulation results. The apparent viscosity was calculated for each injection rate and gas fraction using equation 2.2. Experimental data (points) and history match data (solid lines). Three constant total injection rates were used (rates are indicated with similar colors: 120 mL/h red; 180 mL/h orange; 240 mL/h blue) with the gas fraction varied from f_g = 0.1 to 1.0. In Figure 16, all injection rates reached the maximum apparent viscosity μ_{app} = 3.0, 2.3 and 2.2 cP for the injection rates of 120, 180 and 240 mL/h, respectively, at the same gas fraction, f_g = 0.5. According to equation 2.2, the apparent viscosity is directly proportional to the differential pressure and inversely proportional to the flowrate. However, the change in the flow rate (120 ml/h to 240 ml/h) is greater than the resulting change in the differential pressure, and thus the overall effect of the two parameters is a reduction in viscosity. Table A.2.2 in Appendix A.2 shows apparent viscosity results obtained from experimental and simulation data. Simulation results showed good agreement with the experimental data, which indicates a good match, as shown in Figure 16.

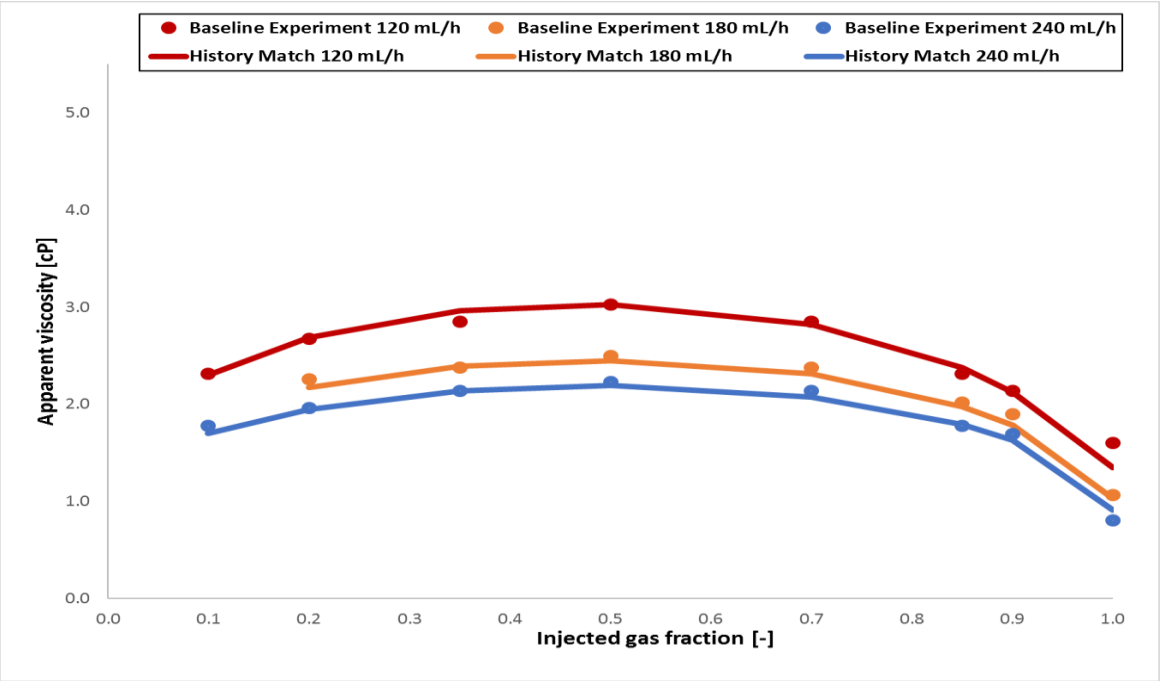

Figure 16: *History match of the baseline apparent viscosity versus gas fraction during the coinjection of CO_2 and brine. Experimental data (points) and the history match (solid lines). Three constant total injection rates used are indicated with similar colors (120 mL/h red; 180 mL/h orange; 240 mL/h blue) with gas fraction varied between f_g = 0.1 and 1.0. The maximum apparent viscosity is observed at f_g = 0.5 in all the three injection rates.*

4.2.2 History Matching the CO_2-NP Foam Quality Scans

This section presents the history match of nanoparticle-stabilized CO_2 foam quality scans. In order to achieve a steady-state during the foam quality scans, a total of 2 PV were injected for each gas fraction with the injection rates of 180 mL/h and 240 mL/h, whereas 6 PV were injected with the rate of 120 mL/h. For history matching, the tuned foam model parameters were FMMOB and the dry-out function, FDRY (Sfdry + Sfbet). Functions including $\mathrm{F1}, \mathrm{F2}, \mathrm{F3}, \mathrm{F4}, \mathrm{F5}, \mathrm{F6}, \text{and } \mathrm{F7}$ were not changed in the history matching. As mentioned earlier, the optimal gas fraction was f_g = 0.7, and thus obtaining a match for this point was crucial.

Foam Differential Pressure - History Match

For the history matching, the reference foam mobility reduction factor (FMMOB) was allowed to vary between 5 and 100, which is the normal range for FMMOB depending on the strength of the created foam (Computer Modelling Group Ltd, 2017). It was found that FMMOB values between 4.4 and 6.7 gave the best match to the experimental data. In the absence of oil, surfactant-stabilized CO_2-foams have been found to be stronger compared to nanoparticle-stabilized foams (Rognmo, 2019). Thus, lower values of FMMOB were selected to represent the nanoparticle-stabilized foam in this work. The allowed range of the maximum foam dry-out (Sfdry) was between 0 and 1, and between 0 and 10^5 for Sfbet (Computer Modelling Group Ltd, 2017). Sfdry values used for the history matching were 0.46 and 0.50. The reference foam dry-out slope (Sfbet) value of 100 was used. As discussed in Chapter 3.2.3, Sfbet controls the sharpness of the transition of foam from a high-quality regime to a low-quality regime; when Sfbet is very large, the transition is sharp and foam collapses within a very narrow range

of water saturation. On the other hand, a low value of Sfbet represents a foam collapse that is not abrupt, where foam coarsens in texture over a range of water saturation (Farajzadeh *et al.*, 2015). According to the same study (Farajzadeh *et al.*, 2015), the value of Sfbet does not influence the results, unless its value is very low. The best match was achieved with the tuned foam model parameters illustrated in Table 4.3.

Table 4. 3*: Estimated Foam model parameters used for history matching.*

Injection Rates [mL/h]	FMMOB	Sfdry	Sfbet
120	4.4	0.46	100
180	5.8	0.5	100
240	6.7	0.5	100

Figure 17 shows results from the experimental work (points) and the history match (solid lines) for different injection rates including 120 mL/h (red), 180 mL/h (orange), and 240 mL/h (blue). By increasing the gas fraction, differential pressure increased by approximately 25 % for all injection rates until f_g = 0.7. The maximum differential pressure at f_g = 0.7 was 30.36, 44.77, and 59.94 kPa for total injection rates of 120, 180, and 240 mL/h, respectively. The differential pressure decreased when gas fraction was above f_g = 0.7, which indicated the transition from the low-quality to the high-quality foam regime. Instability of foam in the high-quality regime (f_g >0.7) is because of the higher gas fraction. Gas fractions in the high-quality regime are a result of foam coalescence and foam dry out. At the highest gas fraction (f_g = 1.0), the model could not capture the experimental points due to trapped gas saturations in the core. Trapped gas occurs in the intermediate-sized pores since the wetting phase (water) occupies the smallest pores (Kovscek and Radke, 1994). By tuning the foam model parameters (FMMOB, Sfdry, and Sfbet), the best match for the differential pressure was achieved. The simulation model was able to match most of the experimental data, as shown in Figure 17. Table A.2.3 in Appendix A.2 also illustrates the above results.

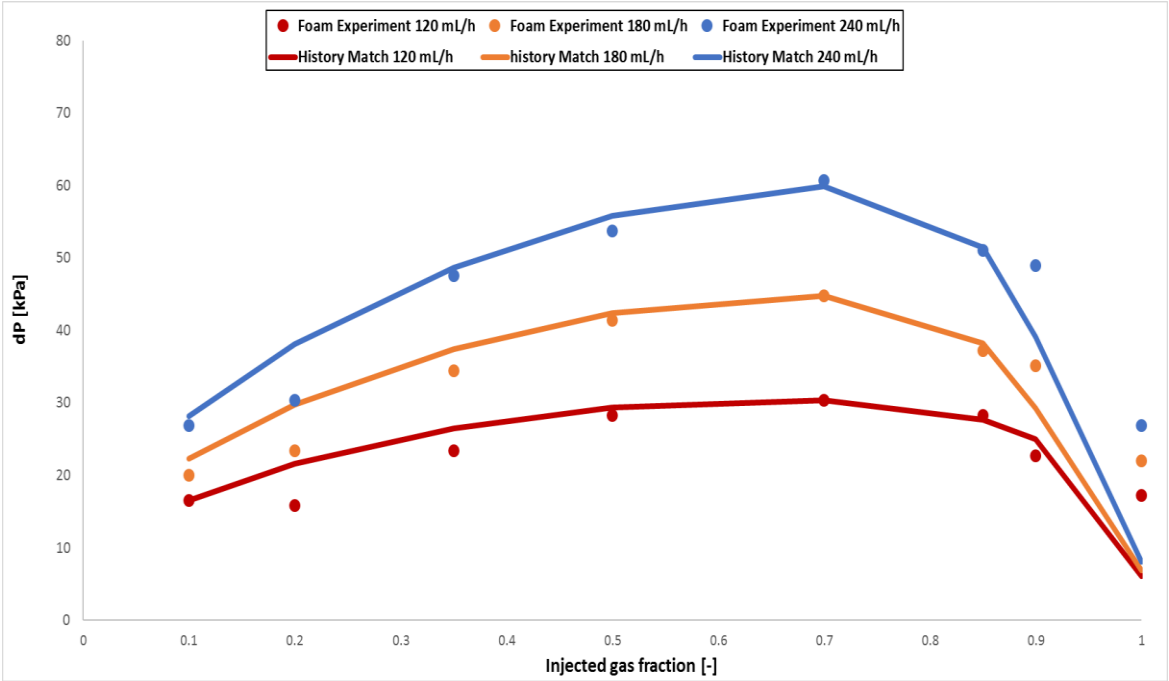

Figure 17: *History match of the steady-state average differential pressure versus gas fraction during the coinjection of NP and CO_2. Experimental data (points) and the history match (solid lines). Three constant total injection rates used are indicated with similar colors (120 mL/h red; 180 mL/h orange; 240 mL/h blue) with gas fraction varied between f_g = 0.1 and 1.0. The maximum differential pressure is observed at f_g = 0.7 in all the three injection rates.*

Apparent CO_2 Foam Viscosity - History Match

Figure 18 shows a comparison of results between the baseline foam quality scans (squared-points and dashed lines) and foam quality scans with nanoparticles present (points and solid lines). Three constant total injection rates are used (rates are indicated with similar colors: 120 mL/h red; 180 mL/h orange; 240 mL/h blue) and the gas fraction varied between f_g = 0.1 and 1.0. The apparent viscosity was calculated from the pressure drop at gas fractions 0.1, 0.2, 0.35, 0.5, 0.7, 0.85, 0.90 and 1.0, with equation 2.2. In the baseline, as discussed in the previous section, the apparent viscosity reached the highest values μ_{app} = 3.0, 2.3, 2.2 cP for the injection rates of 120, 180 and 240 mL/h, respectively, at the gas fraction of 0.5. In CO_2-NP, an increase in apparent viscosity was observed for all three injection rates until f_g = 0.7 was reached, giving the highest value of μ_{app} = 7.8, 7.7 and 7.7 cP for the rates of 120, 180 and 240 mL/h, respectively. The apparent foam viscosity shows an increase of almost 3 times compared to the baseline at the gas fraction of 0.7. The differences in the apparent viscosity between the baseline and the CO_2-NP indicate greater flow resistance (higher apparent viscosity) and foam generation (Ettinger and Radke, 1992).

All foam quality scans used a monotonically increasing gas fraction sequence (drainage-like process) to measure apparent viscosity at each gas fraction. The results from CO_2-NP showed two regions in all the three injection rates. In the low-quality regime (f_g <0.7) , the foam apparent viscosity was monotonically increasing with the foam quality. Once the foam quality passed the low-quality regime and reached the transition point at f_g = 0.7, the foam apparent viscosity started to decrease as the foam quality increased in the high-quality regime (f_g >0.7). This was due to the insight that, in the low-quality regime, the bubble density (or foam texture) increases as a function of foam quality, and thus the apparent viscosity increases. In the high-quality regime, gas mobility rises abruptly over a narrow

range of water saturation because the foam collapses abruptly (Farajzadeh *et al.*, 2015) . This is why, in the high-quality regime, the apparent viscosity decreases as a function of foam quality.

The curved behavior of foam in the high-quality regime due to the high value of the foam parameter Sfbet (dry-out slope) was adjusted by the foam parameter Sfdy (maximum dry-out) for each injection rate in order to match the experimental data. During the foam quality scan, the apparent foam viscosity showed minor differences between flow rates, indicating no shear-thickening behavior (fluid viscosity increases with increasing injection rate) or shear-thinning behavior (fluid viscosity decreases with increasing injection rate). Table A.2.4 in Appendix A.2 lists the foam apparent viscosity values of the experimental and simulation. History matching the apparent foam viscosity during CO_2-NP foam quality scans showed that the model was able to capture the experimental data at the optimal gas fraction (i.e., f_g = 0.7) for all the injection rates. However, experimental foam apparent viscosies at f_g = 1 were unable to be mached. This can be attributed to the presence of trapped gas during the experiment at f_g = 1 and model inability to capture this since no hysteresis relative permeability curves were available.

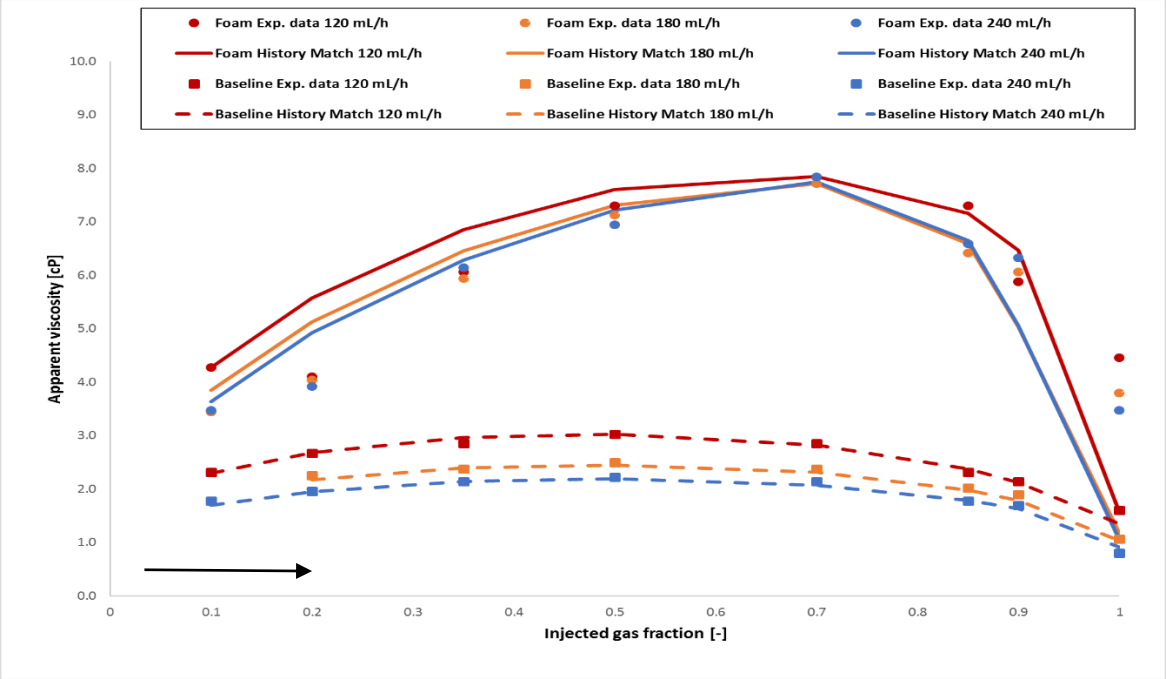

Figure 18: *History match of the apparent CO_2 viscosity versus gas fraction during the co-injections of the baseline and CO_2-NP. The constant total injection rates are indicated with similar colors (120 mL/h red; 180 mL/h orange; 240 mL/h blue). CO_2-NP co-injection (solid line for the history match and points for the experimental data) and baseline (dashed lines for the history match and rectangle-points for the experimental data).The gas fraction varied between f_g = 0.1 and 1.0. A maximum foam apparent viscosity (7.8 cP) was observed at f_g = 0.7, corresponding to almost 3 times higher apparent viscosity compared to the baseline (without nanoparticles). The black arrow points the way the injections were performed with regard to the injected gas fractions.*

Saturation Profiles

Figure 19 shows the model CO_2 and water saturation profiles for CO_2-brine (dashed lines) and CO_2-NP (solid lines) co-injections using the injection rate of 240 mL/h. In the baseline (CO_2-brine), the water saturation (blue dashed line) decreases, and the gas saturation (red dashed line) increases with an increasing gas fraction. In CO_2-NP co-injection, water saturation decreases rapidly. By comparing the baseline with the CO_2-NP co-injection, at the gas fraction (f_g = 0.1 to 0.5), a monotonic linear increase in gas saturation and linear decrease in water saturation was observed for both co-injections. The average gas saturation was s_g = 0.30 and became s_g = 0.44 with CO_2-NP, which indicates an increase of 46.6 % in gas saturation at the same gas fraction of f_g = 0.7. At the same gas fraction, the average water saturation was s_w = 0.70 and decreased to s_w = 0.56, which indicates a decrease of 25 % compared to the baseline. At high gas fractions (f_g = 0.9 to 1.0), the average gas saturation increased significantly and reached final gas saturation s_g = 0.61 compared to s_g = 0.59 in the baseline. The final water saturation with CO_2-NP co-injection was s_w = 0.39 compared to s_w = 0.41 in the baseline. These results indicated that foam is displacing more water from the core, and since baseline viscosity was lower than the viscosity of CO_2-NP, resulted in higher water displacement with CO_2-NP, as shown in Figure 19. Table A.2.5 in Appendix A.2 shows the saturation profiles during the foam quality scans.

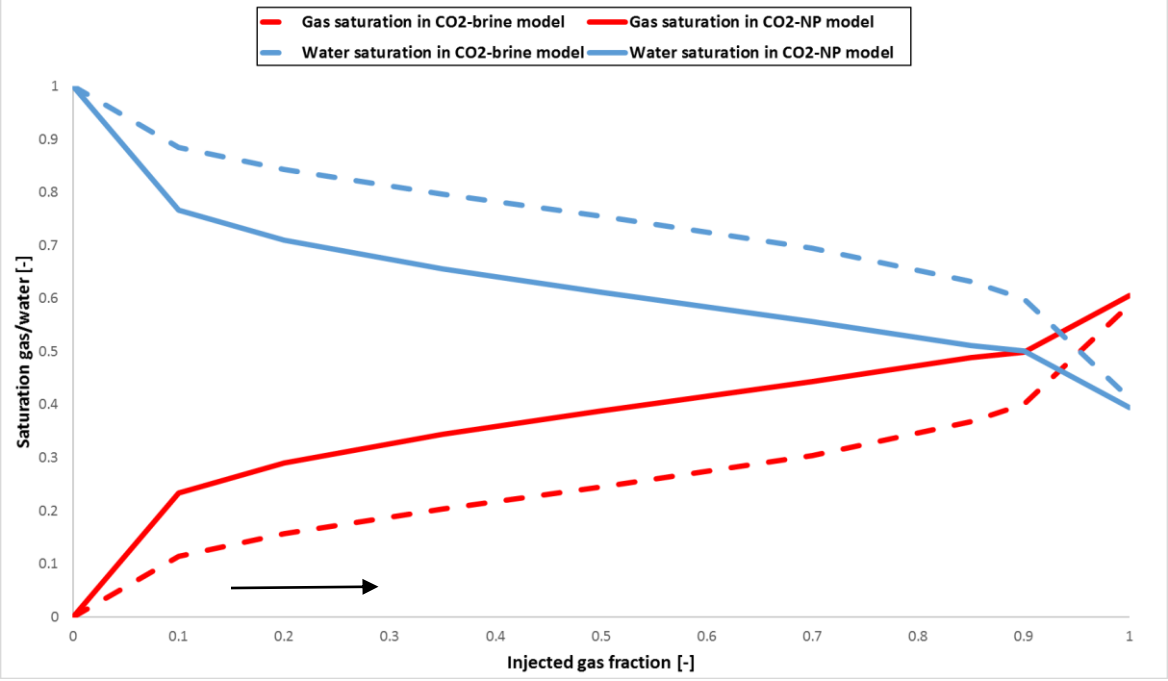

Figure 19: *Saturation profiles versus gas fraction during the co-injections of CO_2-brine (baseline) and CO_2-NP. The total injection rate is 240 mL/h. The baseline (dashed lines) and the CO_2-NP (solid lines). For the baseline (S_w, blue dashed line; S_g, red dashed line) and for the CO_2-NP (S_w, solid blue line; S_g, solid red line). The gas fraction varied between f_g = 0 and 1.0. the arrow points in the direction the injections were performed (increasing gas fraction).*

4.3 Sensitivity Analysis

The sensitivity study was performed to investigate the effect of nanoparticle concentration, FMMOB, Sfdry, Sfbet, the absolute permeability (K), and the total injection rate (Q_T) . The differential pressure and apparent viscosity were investigated versus gas fraction (f_g). The constant total injection rate of 240 mL/h was used in model sensitivity to nanoparticle concentration in the aqueous solution, model sensitivity to the reference foam mobility reduction factor, model sensitivity to the maximum dry-out value, model sensitivity to the reference dry-out slope, and model sensitivity to absolute permeability. The rate of 240 mL/h was used in combination with other injection rates to investigate the effect of velocity on the apparent viscosity and differential pressure during the foam rate scans.

4.3.1 Effect of varying nanoparticle concentration

Figure 20 shows the percentage difference in differential pressure during the foam quality scan with nanoparticles present. The effect of varying nanoparticle concentration at each gas fraction was investigated. Nanoparticle concentrations (i.e., 0.02, 0.15, 0.5, and 1.0 wt%) were investigated for the sensitivity study, where the foam reference case concentration from the experiment was 0.15 wt%. The differential pressure values for different nanoparticle concentrations are listed in Table A.3 in Appendix A.3. A concentration of 0.02 wt% (blue columns) showed the same values as the baseline at gas fractions (0.1 and 0.7). While a percentage decrease of 0.026, 0.021, 0.018, 0.039, 0.026 and 0.123 % was observed at gas fractions 0.2, 0.35, 0.5, 0.85, 0.9 and 1.0, respectively. Increasing nanoparticle concentration to 0.5 wt% (orange columns) resulted in an average increase of 0.059 % for all gas fractions compared to the foam reference case. A concentration of 1.0 wt% (grey columns) gave an average increase of 0.136 % for all gas fractions compared to the reference case. By comparing the results at the transition gas fraction (i.e., 0.7), the percentage differences were 0, 0.033 and 0.083 % for concentrations 0.02, 0.5 and 1.0 wt%, respectively compared to the reference case. In the low-quality regime (f_g <0.7), high nanoparticle concentrations (0.5 and 1.0 wt%) improved their match with reference case results with increasing gas fraction. In contrast, a notable increase in percentage difference was observed in the high-quality regime (f_g >0.7) with increasing the gas fraction. A possible explanation for the nanoparticle behavior in the low-quality regime is that differential pressure increased due to foam generation and propagation. In the high-quality regime, the decrease in differential pressure may be due to rupture of gas bubbles resulting in foam dry-out and bubble coalescence. At the optimal gas fraction (i.e., 0.7), the lowest concentration (0.02 wt%) had a zero percentage difference value, which means the same differential pressure value as the reference case. However, the other concentrations showed gradually increased at the same gas fraction.

The results presented in Figure 20 showed that nanoparticles concentration of 0.02 wt% performed well or equally well, in terms of limited changes in differential pressure, as the reference case concentration of 0.15 wt%. From this investigation, one can conclude that increasing nanoparticles concentration may not result in notably higher values of differential pressure. For further EOR uses, a lower concentration can generate foam, and this is important in terms of economic evaluations and cost-benefit analysis. Table 4.4 lists the percentage difference in the differential pressure for different nanoparticle concentrations. The sensitivity study showed that the model was sensitive to different nanoparticle concentrations.

Table 4. 4: *Percentage difference (Perc.diff) in differential pressure with varying nanoparticles concentration during the foam quality scans.*

		Nanoparticle concentrations		
		0.02 [wt%]	**0.5 [wt%]**	**1.0 [wt%]**
Q_T[mL/h]	fg[-]	Perc.diff[%]	Perc.diff[%]	Perc.diff[%]
240	0.1	0	0.071	0.142
	0.2	-0.026	0.052	0.105
	0.35	-0.021	0.041	0.103
	0.5	-0.018	0.018	0.072
	0.7	0	0.033	0.083
	0.85	-0.039	0.058	0.136
	0.9	-0.026	0.077	0.204
	1	-0.123	0.123	0.246

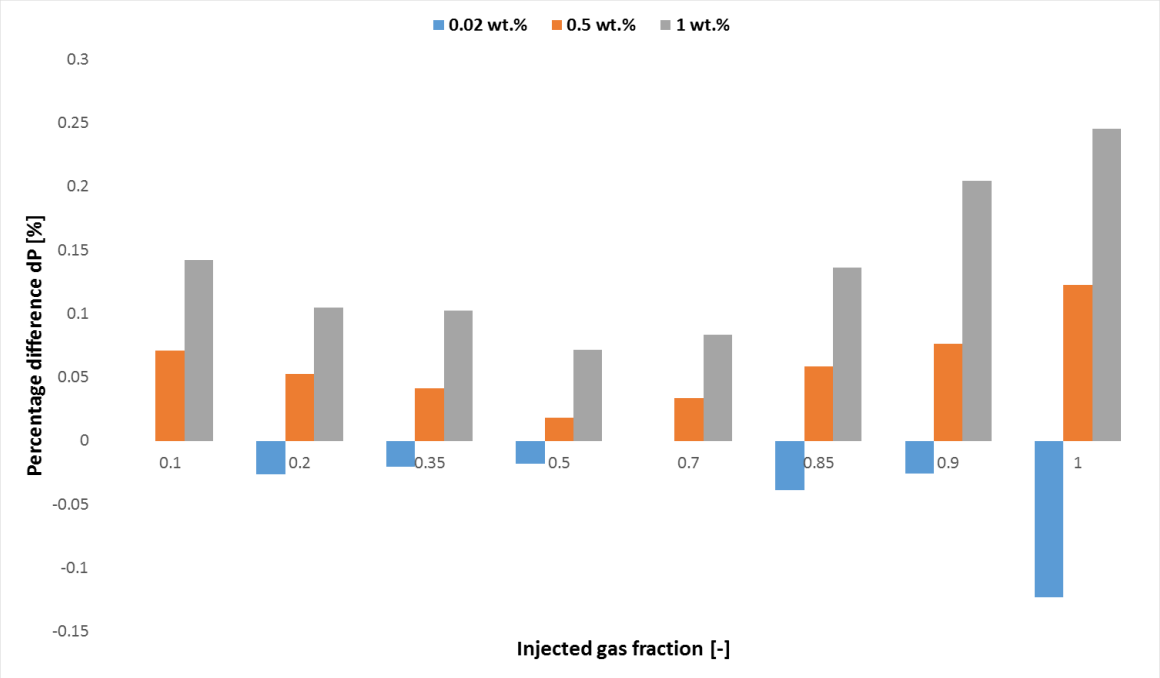

Figure 20*: Foam differential pressure percentage difference versus gas fraction for different nanoparticle concentrations. The total injection rate is 240 mL/h. The columns in blue, orange and grey represent the pressure difference percentage for nanoparticles concentration of 0.02, 0.5 and 1 wt%, respectively.*

4.3.2 Effect of varying reference foam mobility reduction factor, FMMOB

FMMOB is the reference foam mobility reduction factor used in the foam model, and it refers to the maximum gas mobility reduction that can be achieved. As discussed earlier, the value for FMMOB was reduced to 6.7 in order to history match the experimental data since the foaming agent was nanoparticle. Generally, a surfactant-based foam has a higher apparent foam viscosity and requires a larger FMMOB value, whereas a nanoparticle-based foam requires a smaller FMMOB due to lower apparent viscosities. The parameter FMMOB must be used as an input in order to run the foam model. Figure 21 shows the foam apparent viscosity during the foam quality scans with varying FMMOB. Four different values of FMMOB (i.e., 3, 6.7, 10 and 20) were used to investigate the effect of reference foam mobility reduction factor on the foam apparent viscosity. In the foam reference case, FMMOB was equal to 6.7 (blue curve). It can be seen in Figure 21, that an increase in FMMOB increased the foam apparent viscosity at foam qualities (10 to 70 %). At 100 % foam quality (i.e., 100 % gas), the foam apparent viscosity reached the same value for all FMMOB values. When FMMOB was 20, the slope sharply decreased and showed a notable decrease in the apparent viscosity for the foam qualities (70 to 100 %). This decrease in the foam apparent viscosity was due to the fixed dry-out parameters (Sfdry+Sfbet), which were used for all simulation runs. However, the reference foam mobility factor does not impact the transition from low to high-quality regime. The maximum foam apparent viscosity values were achieved at the transition foam quality of 70 % (i.e., 70 % gas and 30 % nanofluid), $\mu_{app} =$ 4.9, 7.7, 9.9 and 14.8 cP for values of FMMOB = 3, 6.7, 10 and 20, respectively, as shown in Figure 21. The results showed that the reference foam mobility reduction factor had a significant impact on the foam apparent viscosity, where foam apparent viscosities increased with increased FMMOB values and decreased with decreased FMMOB values. This gave an indication that the model was highly sensitive to different reference foam mobility reduction values.

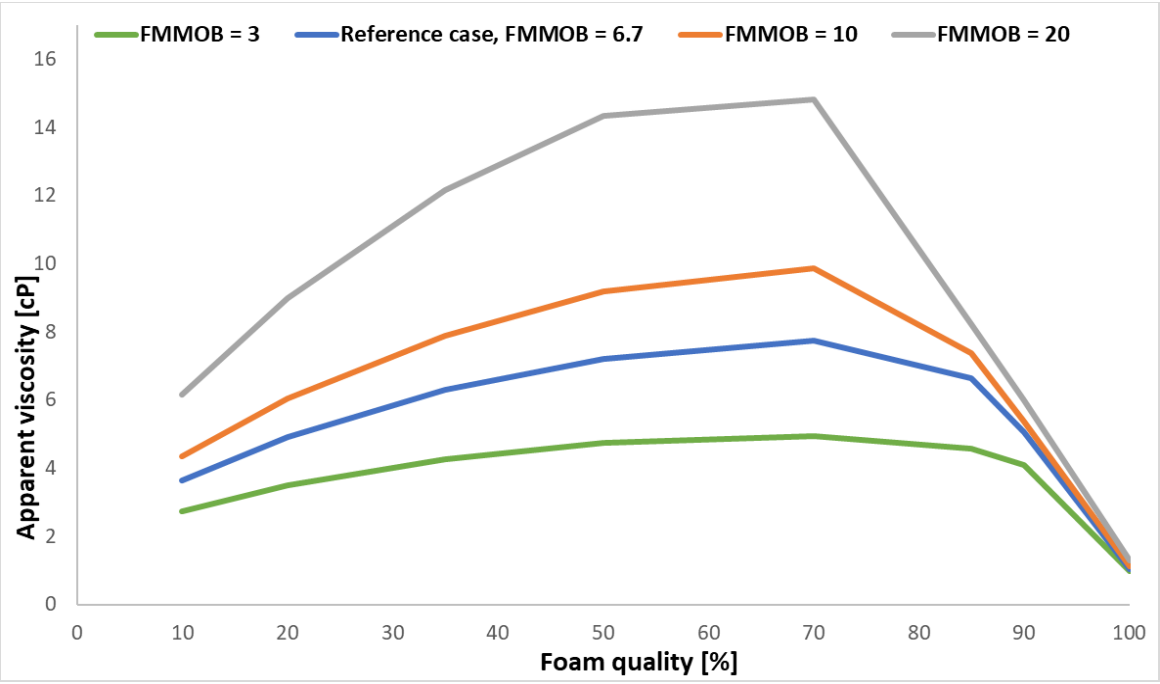

Figure 21: *Foam apparent viscosity profiles versus foam quality with varying FMMOB. The total injection rate is 240 mL/h. The blue curve for the foam reference case (i.e., FMMOB = 6.7), while green, orange and grey colors represent values of FMMOB (i.e., 3, 10 and 20), respectively.*

4.3.3 Effect of varying the maximum dry-out parameter, Sfdry

Figure 22 shows the apparent foam viscosity during the foam quality scans with varying Sfdry. Sfdry is the maximum dry-out value at which foam collapses. The parameter Sfdry corresponds to the limiting water saturation, at which foam begins experiencing significant coarsening (Ma *et al.*, 2013). Two different values of Sfdry = 0.3 and 0.6 were compared to the foam reference case value of 0.5 to investigate the effect of the Sfdry on the apparent viscosity. When Sfdry was 0.6, the apparent viscosity increased with increasing foam quality (gas fractional flow) in the low-quality regime until it reached f_Q = 50 %, where f_Q is the foam quality defined earlier in equation 2.1. At this foam quality, the maximum apparent viscosity value was achieved μ_{app} = 6.7 cP. For f_Q >50 %, the apparent viscosity decreased with increasing foam quality, indicating the beginning of the high-quality regime (foam collapses). When Sfdry was 0.3, the apparent viscosity increased in the low-quality regime until it reached f_Q = 70 %. At this foam quality, the maximum apparent viscosity value μ_{app} = 8.0 cP was achieved. When f_Q became greater than 70 %, the apparent viscosity decreased, indicating the start of the high-quality regime. At the transition point (f_Q = 70 %), the apparent viscosity values became 8.0, 7.7 and 5.0 cP for Sfdry of 0.3, 0.5 and 0.6, respectively. The above results suggested that the dry-out parameter Sfdry influenced only the high-quality regime. The results showed that the maximum dry-out parameter Sfdy had a significant impact on the foam apparent viscosity in the high-quality regime, where foam apparent viscosities decreased with increased Sfdry values and increased with decreased Sfdry values.

A higher value of Sfdry starts the high-quality regime earlier compared to lower. The transition water saturation was 0.56, and this value was found from the saturation profiles discussed earlier in Chapter 4.2.2. According to the previous study, the value of Sfdry should be lower than the transition water saturation (Ma *et al.*, 2013). The sensitivity analysis showed that the model was highly sensitive to different Sfdry values in the high-quality regime.

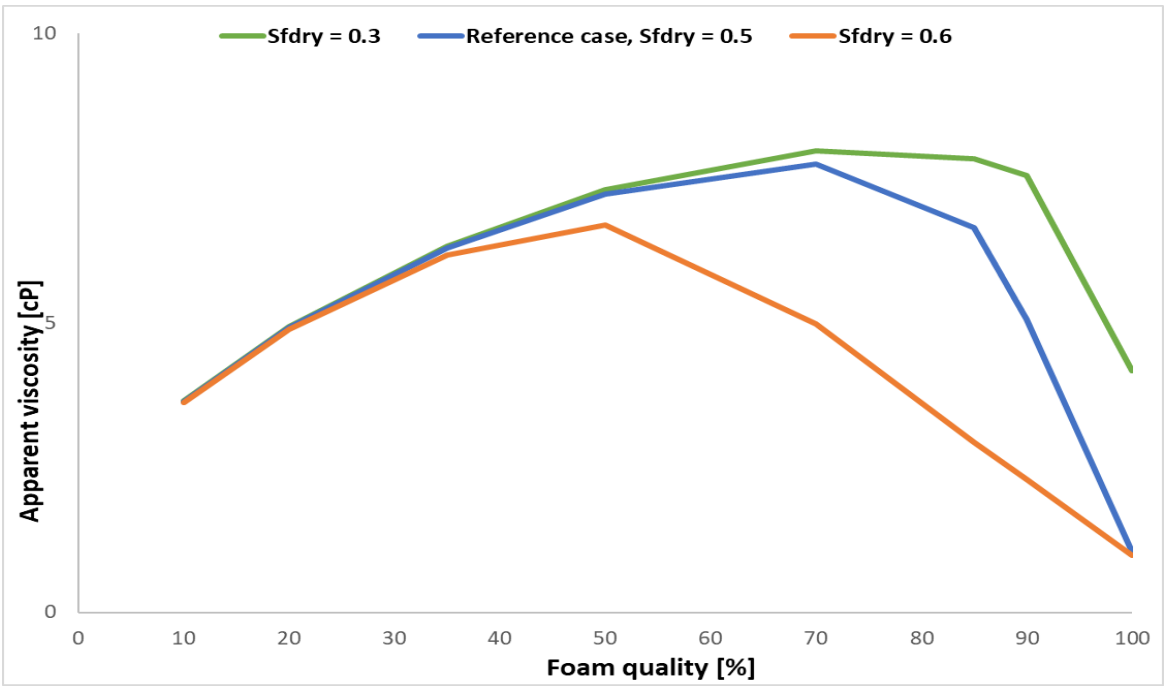

Figure 22: *Foam apparent viscosity versus foam quality with varying Sfdry. The total injection rate is 240 mL/h. Foam reference case (Sfdry = 0.5, blue curve), Sfdry = 0.3 (green curve) and Sfdry = 0.6 (orange curve).*

4.3.4 Effect of varying the reference dry-out slope, Sfbet

Figure 23 shows the apparent foam viscosity during the foam quality scans with varying Sfbet. Sfbet is foam collapse abruptness parameter in the foam model. The parameter Sfbet regulates the slope of FDRY curve near Sfdry in order to control the collapse rate of foam. A large Sfbet value indicates that foam dries out sharply, whereas small Sfbet value indicates that foam dries out more gradually (Ma *et al.*, 2013), Sfbet = 100 was used in the foam reference case (green curve). Two other values of Sfbet were used, namely Sfbet = 10 and 1000. Sfbet = 10 showed decreasing in the slope in both low-quality and high-quality regimes, resulting in decreased apparent foam viscosity (blue curve) in both regimes. The maximum apparent viscosity value achieved by Sfbet = 10 is μ_{app} = 6.4 cP which was lower than the foam reference case apparent viscosity (μ_{app} = 7.7 cP) at the same foam quality (f_Q = 70 %). At foam qualities from f_Q= 90 to 100 %, the apparent viscosity showed a higher value compared to the foam reference case. When Sfbet was 1000, the apparent viscosity (orange curve) showed similar values in the low-quality regime for foam qualities (10 to 35 %) compared to the foam reference case. At the foam quality of 70 %, the maximum apparent viscosity value μ_{app} = 8.0 cP was achieved, which was higher than the foam reference case. In the high-quality regime, the foam viscosity also showed higher values for foam quality between 70 and 90 %. At foam qualities between 90 and 100 %, the apparent viscosity showed similar values of the foam reference case. This gives an indication that a higher value of Sfbet results in better matching compared to the lower value (Sfbet = 10). The results showed that the maximum dry-out slope Sfbet had a significant impact on the foam apparent viscosity in both the high-quality and the low-quality regime, where foam apparent viscosities increased with increased Sfbet values and decreased with decreased Sfbet values. It was observed that reducing the value of Sfbet may influence the results. One can conclude that the model was moderately sensitive to the changes in Sfbet values.

Figure 23: *Foam apparent viscosity versus foam quality with varying Sfbet. The total injection rate is 240 mL/h. Foam reference case (Sfbet = 100, green curve), Sfbet = 10 (blue curve) and Sfbet = 1000 (orange curve).*

4.3.5 Effect of varying the absolute permeability, K

Figure 24 shows the average differential pressure during foam quality scans for two different absolute permeability values. Note that only absolute permeability changed in each simulation run, while the relative permeability curves remain the same. The total injection rate was 240 mL/h. Absolute permeability values (i.e., 1000 and 500 mD) were investigated. The foam reference pressure (solid green line) is shown for absolute permeability K = 2252 mD, which was the experimental value. When the absolute permeability was reduced to K = 1000 mD (solid orange line), a higher pressure value ΔP = 107 kPa was achieved compared to the foam reference case ΔP = 47.4 kPa with an increase of 59.9 kPa at the same gas fraction f_g = 0.7. When the absolute permeability was further reduced to 500 mD (solid blue line), the pressure became 215 kPa, which indicated an increase of 167.6 kPa compared to the foam reference case at f_g = 0.7. The increase in the differential pressure can be explained by the permeability differences in the three cases. The lowest permeability resulted in the highest differential pressure.The baseline foam quality scans (dashed lines) also showed increased differential pressure with decreased absolute permeability, as shown in Figure 24.

In general, the absolute permeability has an influence on the apparent viscosity since the calculation of apparent viscosity accounts for the permeability of the rock. Relative permeability is the tuning parameter in all history matching and its an input in the simulator as a table (fixed values). However, since the relative permeability is the ratio of effective permeability and absolute permeability, then changing only the absolute permeability will affect the differential pressure behavior, while the viscosity will remain unchanged. The differential pressure increased with decreased permeability as expected, and the model was highly sensitive to different absolute permeability values.

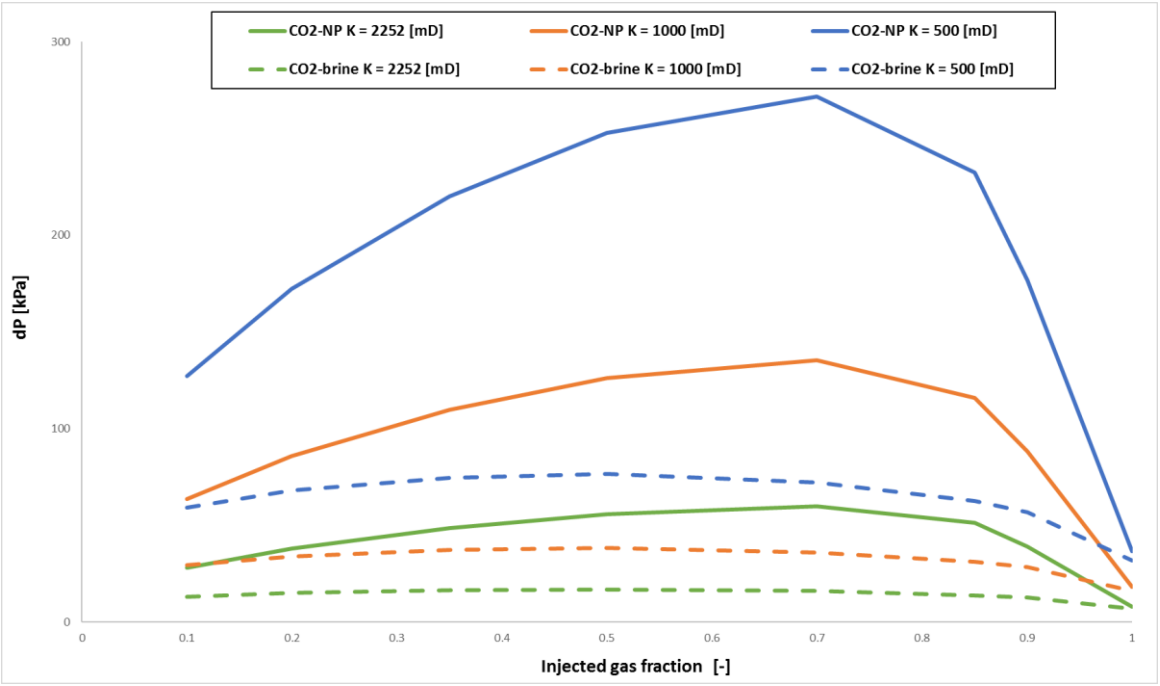

Figure 24: *Average differential pressure versus gas fraction during the CO_2-NP foam quality scans (solid lines), and the baseline foam quality scans(dashed lines). Three different absolute permeability values (2252 mD; green, 1000 mD; orange and 500 mD; blue).*

4.3.6 Effect of varying the total injection rate, Q_T

Figure 25 shows the apparent foam viscosity with varying injection velocity during the foam rate scans. The foam rate scan was conducted separately at gas fractions (0.7 and 0.85). The gas fraction 0.7 was the optimal gas fraction estimated from the foam quality scans in which the apparent foam viscosity achieved the highest values for all injection rates. The total injection rate was increased from 120 mL/h to 500 mL/h. Each injection rate achieved stable differential pressure at the gas fraction. At gas fraction of 0.7, the differential pressure had a total average increase of 23.8 kPa for all the injection rates. When the gas fraction was increased to 0.85, the differential pressure had a total average increase of 20.4 kPa for all the injection rates. This indicates that differential pressure decreasing with increasing the gas fraction, as shown in Table 4.5. The results also showed limited changes in foam apparent viscosity with changes in superficial velocities, as shown in Table 4.5. As seen in Figure 25, no shear-thinning behavior (decreasing apparent viscosity with increasing injection rate) or shear-thickening (increasing apparent viscosity with increasing injection rate) was observed. The nanoparticle-stabilized CO_2-foam showed a near-Newtonian behavior since the apparent viscosities were almost constants for all the injection velocities, as shown in Figure 25. The experimental work was conducted by Rognmo et al. (2017) on CO_2-NP foam apparent viscosity also showed a near-Newtonian behavior, and this is an indication that the model was agreed with the experimental work. In the case of surfactant-based foam, a decrease in foam apparent viscosity with increasing the injection velocities is expected behavior due to shear-thinning flow (Lee et al., 1991; Sheng, 2013a). The sensitivity analysis during the foam rate scans confirmed the accuracy of the results conducted in the experimental work.

Table 4. 5: *Foam apparent viscosity and differential pressure during the foam rate scans.*

f_g [-]	Q_T [mL/h]	$\mu_{app,Simu.}$ [cP]	ΔP [kPa]
0.7	120	7.74	29.94
	180	7.74	44.94
	240	7.74	59.94
	300	7.75	74.96
	500	7.76	125.13
0.85	120	6.64	25.71
	180	6.65	38.63
	240	6.59	51.42
	300	6.64	64.33
	500	6.65	107.31

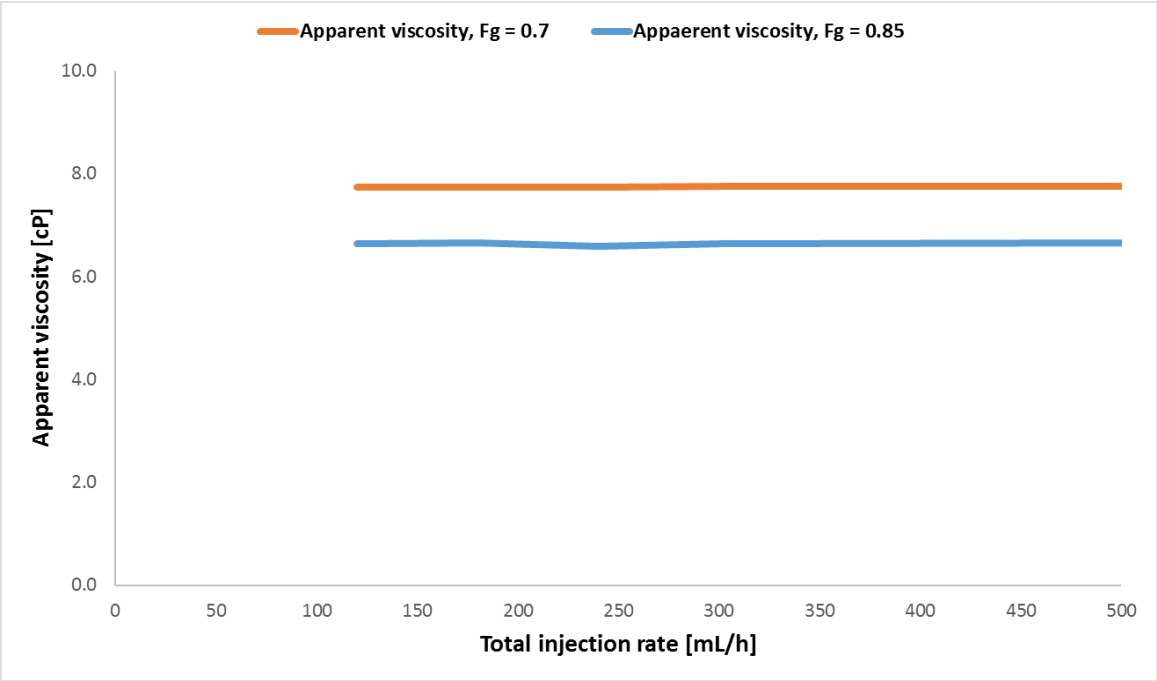

Figure 25 : *Foam apparent viscosity versus injection rate during the foam rate scans with nanoparticles present. The total injection rate was increased from 120 mL/h to 500 mL/h. A constant apparent viscosity for increased injection rates indicates no shear-thinning or shear-thickening behaviors. Apparent viscosity at gas fraction 0.7 (orange) and at gas fraction 0.85 (blue).*

Sensitivity Analysis Main Findings

The sensitivity analysis investigated the effect of foam model parameters and their impact on apparent viscosity. The sensitivity analysis showed that the reference foam mobility reduction factor (FMMOB) had a significant impact on the foam apparent viscosity, where foam apparent viscosities were closely linked and proportional with changes in FMMOB. However, the reference foam mobility reduction factor did not impact the transition from low to high-quality regime. It was observed that the maximum dry-out parameter, Sfdy, had a significant impact on the foam apparent viscosity in the high-quality regime, where foam apparent viscosities decreased with increased Sfdry values and increased with decreased Sfdry values. This was due to the dry out effect where foam dried (foam coalescence). It was also observed that the maximum dry-out slope, Sfbet, had a significant impact on the foam apparent viscosity in both the high-quality and the low-quality regime, where foam apparent viscosity increased with increased Sfbet values and decreased with decreased Sfbet values. One can conclude that the model was highly sensitive to the changes in both FMMOB and Sfdry values and moderately sensitive to the changes in Sfbet values.

Chapter 5: Conclusions and Future Work

5.1 Conclusions

A local-equilibrium foam model, precisely the default model of the compositional EOS simulator CMG-GEM, was utilized in this study. However, some modifications were necessary in order to match the experimental data. The model represented the effect of reference foam reduction factor (FMMOB) and the dry-out function FDRY (Sfdry + Sfbet) on steady-state foam flow. The relative permeability curves were obtained in the form of Modified Brooks Corey parameters and used as inputs in the model. The results obtained in this simulation study were consistent with the theory discussed earlier in the thesis.

History matching of the experimental data followed by sensitivity study were conducted and confirmed that GEM is adequate for modeling nanoparticle-based foam. The co-injection of CO_2 and nanofluid showed a constant apparent foam viscosity with increasing the total injection rate, as Rognmo et al. (2017) stated in their research, and as discussed in Chapter 3.1. From the experimental work, the maximum apparent viscosity of 7.8 cP was observed at a foam quality of 70 % (i.e., 70 % CO_2 and 30 % nanofluid) for all injection velocities. In addition, it was observed that nanoparticles in brine solution were able to generate and stabilize CO_2-foam.

The model was capable of reproducing the experimental observations in the baseline foam quality scans (CO_2 + brine), whereas history matching the foam quality scans with nanoparticles present was with an emphasis on the optimal gas fraction f_g = 0.7. For the baseline foam quality scans, the model was able to match all the experimental data where the maximum apparent viscosity was achieved at gas fraction of 0.5 for all injection velocities. From CO_2-NP foam quality scans, it was observed that the apparent viscosity increased to a maximum value (7.7 cP) at f_g = 0.7, which is the transition for the low-quality regime (f_g <0.7) to the high-quality regime (f_g >0.7), whereas, for baseline foam quality scans (without nanoparticles), the apparent viscosity was almost 3 times lower compared with the foam quality scans of CO_2-NP at the same gas fraction. This indicated foam generation and that nanoparticles stabilized CO_2 foam. No shear-thickening behavior (fluid viscosity increases with increasing injection rate) or shear-thinning behavior (fluid viscosity decreases with increasing injection rate) was observed during the foam scanning. The model saturation profiles indicated that foam was displacing more water from the core, and since baseline viscosity was lower than the viscosity of CO_2-NP, resulted in higher water displacement with CO_2-NP compared to the baseline.

The sensitivity study was performed on the foam model parameters, including the reference foam mobility reduction factor, the maximum dry-out foam parameter, and the dry-out slope. History-matched data with the injection rate of 240 mL/h were the foam reference case in the sensitivity analysis. Nanoparticle concentration and the injection velocity were also investigated in order to understand how uncertain model parameters impact the simulation results, including differential pressure and apparent viscosity. Nanoparticle concentration of 0.02 wt% was able to generate CO_2-foam with differential pressure behavior closely matching the behavior from the reference case at all gas fractions. The highest percentage difference was at gas fraction f_g = 1 and it didn't exceed 0.15 %. However, the apparent viscosity was sensitive to the variation of the gas fraction. The reference foam mobility reduction factor, FMMOB, had a significant impact on the foam apparent viscosity, where foam apparent viscosities increased with increased FMMOB values and decreased with decreased FMMOB values. The maximum dry-out parameter, Sfdy, had a significant impact on the foam apparent viscosity in the high-quality regime, where foam apparent viscosities decreased with increased Sfdry

values and increased with decreased Sfdry values. The maximum dry-out slope, Sfbet, had an impact on the foam apparent viscosity in both the high-quality and the low-quality regime, where foam apparent viscosities increased with increased Sfbet values and decreased with decreased Sfbet values. Foam rate scans showed that the foam apparent viscosity was nearly constant with changes in the injection velocities at gas fractions of 0.7 and 0.85. The nanoparticle-stabilized CO_2-foam showed a near-Newtonian behavior with limited changes in foam apparent viscosity with changes in the total injection rates (superficial velocities). Comparing the parameters obtained through matching of the experimental data, it was observed that for this given system, foam stability was highly sensitive to different foam model parameters, including the reference foam mobility reduction factor and the dry out function. Considering the unavoidable uncertainty, this study demonstrated that the model provided a reasonable and reliable history match. Moreover, the applied history matching methodology was appropriate to tune uncertain model parameters to reproduce experimental observations.

5.2 Future Work

The work confirmed that CMG-GEM was an adequate simulator for modeling of core flood experiments with co-injections of CO_2-brine and CO_2-NP. In this thesis, an investigation into local-equilibrium foam modeling based on foam scanning was performed. However, there are several non-tested options should be further investigated. This gave rise to several ideas for future work:

- The model should be expanded to allow for investigating the effect of the trapped-gas fraction on foam generation.
- An updated model should allow for investigating the effect of oil on foam generation where the defoaming action of the oil still not fully understood.
- Investigating the dependence of foam stability on parameters including temperature, salinity, wettability, and oil composition.
- It would also be interesting to investigate the effect of grid resolution by creating 2D and 3D model to replicate the core-flooding experiment in order to investigate the accuracy and reproducibility of the 1D model.
- Upscaling this core flood model to field-scale model with deriving the foam parameters would be an exciting subject.

Appendix A: Foam Mathematical Model, History Match Data and The Effect of Nanoparticle Concentration

A.1: Foam Mathematical model

Foam Mathematical model discussed in Chapter 3.2.3.

Table A. 1: *Foam Mathematical Model.*

Model	Description
$k_{rg}^{f} = k_{rg} \times FM$	k_{rg}^{f}: foam relative permeability k_{rg}: gas relative permeability FM: mobility reduction factor
$FM = \frac{1}{1 + FMMOB(F1 \times F2 \times F3 \times F4 \times F5 \times F6 \times F7 \times FDRY)}$	fmmob: Reference foam mobility reduction factor
$F1 = \left(\frac{MOLE\ FRACTION(ICPREL)}{FMSURF}\right)^{EPSURF}$	fmsurf: Critical component mole fraction value
$F2 = \left(\frac{(FMOIL - OIL\ SATURATION)}{(FMOIL - FLOIL)}\right)^{EPOIL}$	fmoil: Critical oil saturation value
$F3 = \left(\frac{FMCAP}{CAPILLARY\ NUMBER}\right)^{EPCAP}$	fmcap: Reference rheology capillary number value
$F4 = \left(\frac{(CAPILLARY\ NUMBER - FMGCP)}{FMGCP}\right)^{EPCPG}$	fmgcp: Critical generation capillary number value
$F5 = \left(\frac{(FMOMF - X_{COMP\_NAME})}{FMOMF}\right)^{EPOMF}$	fmomf: Critical oil mole fraction for component 'comp_name'
$F6 = \left(\frac{(X_{SALT} - FSALT)}{(FMSALT - FLSALT)}\right)^{EPSALT}$	fmsalt: Critical salt mole fraction value
$F7 = \left(\frac{1}{FMPERM1}\right) \times \ln\left(\left(\frac{PERMAV}{FMPERM2}\right) + 1\right)$	fmperm1: permeability dependence parameter 1. Fmperm2: permeability dependence parameter 2.
$FDRY = 0.5 + \frac{\arctan(sfbet(S_w - sfdry))}{\pi}$ Where, $sfdry = \max(Q1, Q2, Q3, Q4)$, with, $Qn = Gn \times (1 - sfdry) + sfdry,\ n = 1,2,3,4$, and $G1 = \left(\frac{sfsurf - Mole\ Fraction\ (icprel)}{sfsurf}\right)^{efsurf}$	fdry: foam dry-out parameter. sfbet: Reference dry-out slope. sfdry: Max. dry-out value.

$G2 = \left(\frac{S_o - sfoil}{abs(sfoil - sloil)}\right)^{efoil}$ $G3 = \left(\frac{sfcap}{(capillary\ number)}\right)^{efcap}$ $G4 = \left(\frac{(sfsalt - Salt\ Mole\ Fraction)}{(sfsalt - slsalt)}\right)^{efsalt}$ $S_w = Water\ saturation\ in\ the\ grid\ block$ $S_o = Oil\ saturation\ in\ the\ grid\ block$	

A.2: Differential pressure, apparent viscosity and saturation profiles data during the foam quality scans

Table A. 2.1: Average differential pressure data for experiment and simulation during the baseline foam quality scans.

		Experimnetal	Simulation
Injection Rate [mL/h]	fg [-]	dp [kPa]	dp [kPa]
120	0.1	8.96	8.89
	0.2	10.34	10.39
	0.35	11.03	11.47
	0.5	11.72	11.72
	0.7	11.03	10.91
	0.85	8.96	9.19
	0.9	8.27	8.23
	1	6.21	5.21
180	0.2	13.10	12.61
	0.35	13.79	13.89
	0.5	14.48	14.23
	0.7	13.79	13.42
	0.85	11.72	11.47
	0.9	11.03	10.38
	1	6.21	6
240	0.1	13.79	13.16
	0.2	15.17	15.08
	0.35	16.55	16.56
	0.5	17.24	16.97
	0.7	16.55	16.03
	0.85	13.79	13.87
	0.9	13.10	12.63
	1	6.21	7.07

Table A. 2.2: Apparent viscosity data for experiment and simulation during the baseline foam quality scans.

		Experimental	Simulation
Injection Rate [mL/h]	fg [-]	μ app [cP]	μ app [cP]
120	0.1	2.3	2.3
	0.2	2.7	2.7
	0.35	2.9	3.0
	0.5	3.0	3.0
	0.7	2.9	2.8
	0.85	2.3	2.4
	0.9	2.1	2.1
	1	1.6	1.3
180	0.2	2.3	2.2
	0.35	2.4	2.4
	0.5	2.5	2.5
	0.7	2.4	2.3
	0.85	2.0	2.0
	0.9	1.9	1.8
	1	1.1	1.0
240	0.1	1.8	1.7
	0.2	2.0	1.9
	0.35	2.1	2.1
	0.5	2.2	2.2
	0.7	2.1	2.1
	0.85	1.8	1.8
	0.9	1.7	1.6
	1	0.8	0.9

Table A. 2.3: Average differential pressure data for experiment and simulation during the foam quality scans with nanoparticles present.

		Experimental	Simulation
Injection Rate [mL/h]	fg [-]	dp [kPa]	dp [kPa]
120	0.1	16.55	16.53
	0.2	15.86	21.58
	0.35	23.44	26.53
	0.5	28.27	29.41
	0.7	30.34	30.36
	0.85	28.27	27.71
	0.9	22.75	25.04
	1	17.24	6.11
180	0.1	19.99	22.36
	0.2	23.44	29.76
	0.35	34.47	37.47
	0.5	41.37	42.43
	0.7	44.82	44.77
	0.85	37.23	38.22
	0.9	35.16	29.25
	1	22.06	7
240	0.1	26.89	28.17
	0.2	30.34	38.1
	0.35	47.57	48.67
	0.5	53.78	55.85
	0.7	60.67	59.94
	0.85	51.02	51.43
	0.9	48.95	39.16
	1	26.89	8.14

Table A. 2.4: Foam apparent viscosity data for experiment and simulation during the foam quality scans with nanoparticles present.

		Experimental	Simulation
Injection Rate [mL/h]	fg [-]	μ app [cP]	μ app [cP]
120	0.1	4.3	4.3
	0.2	4.1	5.6
	0.35	6.1	6.9
	0.5	7.3	7.6
	0.7	7.8	7.8
	0.85	7.3	7.2
	0.9	5.9	6.5
	1	4.5	1.6
180	0.1	3.4	3.9
	0.2	4.0	5.1
	0.35	5.9	6.5
	0.5	7.1	7.3
	0.7	7.7	7.7
	0.85	6.4	6.6
	0.9	6.1	5.0
	1	3.8	1.2
240	0.1	3.5	3.6
	0.2	3.9	4.9
	0.35	6.1	6.3
	0.5	6.9	7.2
	0.7	7.8	7.7
	0.85	6.6	6.6
	0.9	6.3	5.1
	1	3.5	1.1

Table A. 2.5: History matching saturation profiles data with a total injection rate of 240 mL/h.

	Baseline Foam quality scan		**CO_2-NP foam quality scan**	
F_g	**S_w**	**S_g**	**S_w**	**S_g**
0	1	0	1	0
0.1	0.89	0.11	0.77	0.23
0.2	0.84	0.16	0.71	0.29
0.35	0.80	0.20	0.66	0.34
0.5	0.76	0.24	0.61	0.39
0.7	0.70	0.30	0.56	0.44
0.85	0.63	0.37	0.51	0.49
0.9	0.60	0.40	0.50	0.50
1	0.41	0.59	0.39	0.61

A.3: The effect of nanoparticle concentration

Table A.3 shows the effect of nanoparticle concentration on foam differential pressure discussed in Chapter 4.3.1, where the foam reference case was at 1500 ppm (equivalent to 0.15wt.%) and three other concentrations (0.02, 0.5 and 1.0 wt%) to see the behavior of nanoparticle concentration on the average differential pressure.

Table A. 3: *Average differential pressure data with varying nanoparticle concentrations during the foam quality scans with nanoparticles present.*

		Nanoparticle concentrations [wt%]			
		0.02	0.15	0.5	1
Q [mL/h]	Fg[-]	dP[kPa]	dP[kPa]	dP[kPa]	dP[kPa]
240	0.1	28.17	28.17	28.19	28.21
	0.2	38.09	38.1	38.12	38.14
	0.35	48.66	48.67	48.69	48.72
	0.5	55.84	55.85	55.86	55.89
	0.7	59.94	59.94	59.96	59.99
	0.85	51.41	51.43	51.46	51.5
	0.9	39.15	39.16	39.19	39.24
	1	8.13	8.14	8.15	8.16

Appendix B: Sample Input Data

B.1 An example of GEM Input File - CO_2-NP co-injection of core ST3

The following is an input data file for CMG GEM simulator. These data were used for history matching of CO_2 and nanofluid co-injection in Chapter 4.

```
** 2019-07-15, 13:59:16, sah005
** 2019-07-15, 19:05:23, sah005
RESULTS SIMULATOR GEM 201710

*TITLE1 'Foam Modeling'
*TITLE2 'Fmmob'
*CASEID 'FOAM-MOD'

INUNIT SI
*WRST 0
*WSRF *GRID *TIME
WSRF WELL 1

** OUTSRF *SPECIAL *DROP 1 1 1  50 1 1
*OUTPRN *GRID *IMPL *PRES *SO *SG *SW *FMC7PERM *KRINTER
*OUTPRN *RES *ALL
*OUTSRF *WELL *PAVG
*OUTSRF *WELL *LAYER *ALL
*OUTSRF *GRID *PRES *SO *SG *SW *KRO *KRG *KRW *MOLALITY 'Surf'
      *VISO *VISG *VISW *CAPNGW *KRINTER W 'Surf' *ADS 'Surf'
      *FMC1SURF *FMC2COIL *FMC3CAPN *FMC4GCAPN *FMC5OMF *FMC6SALT *FMC7PERM
      *FMCDRYOUT *CAPNGW *SIGMAGW
*DIARY *WELL-INFO

** --------------------------------- GRID AND RESERVOIR DEFINITION ---------------------------------
GRID VARI 50 1 1
```

```
KDIR DOWN
DI IVAR
 50*0.00576
DJ JVAR
 0.03341075509
DK ALL
 50*0.03341075509
DTOP
 50*1
**  0 = pinched block, 1 = active block
PINCHOUTARRAY CON           1
**  0 = null block, 1 = active block
NULL CON           1
POR CON         0.2381
PERMI CON         2252
PERMJ  EQUALSI
PERMK  EQUALSI
CPOR 2.5e-20

** ----------------------------------FLUID COMPONENT DATA--------------------------

MODEL PR
NC 2 2
COMPNAME 'CO2' 'NC10'

HCFLAG
0 1
TRES 20.00000
*PHASEID *GAS
PVC3 1.20000000E+00
VISCOR HZYT
```

MIXVC 1.0000000E+00

VISCOEFF

1.0230000E-01 2.3364000E-02 5.8533000E-02 -4.0758000E-02 9.3324000E-03

MW

4.4010000E+01 1.3400000E+02

AC

2.2500000E-01 4.4377400E-01

PCRIT

7.2800000E+01 2.5010000E+01

VCRIT

9.4000000E-02 5.2100000E-01

TCRIT

3.0420000E+02 6.2210000E+02

** VISCOR MODPEDERSEN

** VISCOEFF

** 1.3040000E-04 2.3030000E+00 7.3780000E-03 1.8470000E+00 5.1730000E-01

PCHOR

7.8000000E+01 3.8191680E+02

SG

8.1800000E-01 7.8200000E-01

TB

-7.8450000E+01 1.6585000E+02

OMEGA

4.5723553E-01 4.5723553E-01

OMEGB

7.7796074E-02 7.7796074E-02

VSHIFT

0.0000000E+00 0.0000000E+00

VISVC

9.4000000E-02 5.2100000E-01

BIN

1.1500000E-01

ENTHCOEF

9.6880000E-02 1.5884300E-01 -3.3712000E-05 1.4810500E-07 -9.6620300E-11 2.0738320E-14

0.0000000E+00 -4.4918993E-02 4.2590035E-04 -6.4079614E-08 0.0000000E+00 0.0000000E+00

*DENWS 1010 ** kg/m3 ** Suface water density

*CW 4.35E-013 ** 1/kpa ** water compressibility

*REFPW 101.325 ** kpa ** ref. pressure

*VISW 1.03 ** cp ** water visicosity

*NC-AQUEOUS 1

*COMPNAME-AQUEOUS 'Surf'

*MW-AQUEOUS 60.8

*AQUEOUS-DENSITY *ROWE-CHOU

*COMPNAME-SURFACTANT 'Surf'

** ---------- ROCK-FLUID DATA ----------

*ROCKFLUID

RPT 1

*FOAM-MODEL *MULTREL

*FMCOMP 'Surf'

*FMMOB 6.7

*SFDRY 0.5

*SFBET 100

SGT

** Sg krg krog

0 0 1

0.04 0.000591683 0.857375

0.08 0.002060361 0.729

0.12 0.004274719 0.614125

0.16 0.007174594 0.512

0.2 0.010721002 0.421875

0.24 0.014885438 0.343

0.28 0.019645624 0.274625

0.32 0.024983388 0.216

0.36 0.030883455 0.166375

0.4 0.037332697 0.125

0.44 0.044319637 0.091125

0.48 0.051834105 0.064

0.52 0.059866986 0.042875

0.56 0.068410037 0.027

0.8 0.13 0

SWT

** Sw krw krow

0.2 0 1

0.21 2.44141E-08 0.97515625

0.22 3.90625E-07 0.950625

0.23 1.97754E-06 0.92640625

0.24 6.25E-06 0.9025

0.25 1.52588E-05 0.87890625

0.26 3.16406E-05 0.855625

0.27 5.86182E-05 0.83265625

0.28 0.0001 0.81

0.29 0.000160181 0.78765625

0.3 0.000244141 0.765625

0.31 0.000357446 0.74390625

0.32 0.00050625 0.7225

0.33 0.00069729 0.70140625

0.34 0.000937891 0.680625

0.35 0.001235962 0.66015625

0.36 0.0016 0.64

0.37 0.002039087 0.62015625

0.38 0.002562891 0.600625

0.39 0.003181665 0.58140625

0.4 0.00390625 0.5625

0.41 0.004748071 0.54390625

0.42 0.005719141 0.525625

0.43 0.006832056 0.50765625

0.44 0.0081 0.49

0.45 0.009536743 0.47265625

0.46 0.011156641 0.455625

0.47 0.012974634 0.43890625

0.48 0.01500625 0.4225

0.49 0.017267603 0.40640625

0.5 0.019775391 0.390625

0.51 0.022546899 0.37515625

0.52 0.0256 0.36

0.53 0.028953149 0.34515625

0.54 0.032625391 0.330625

0.55 0.036636353 0.31640625

0.56 0.04100625 0.3025

0.57 0.045755884 0.28890625

0.58 0.050906641 0.275625

0.59 0.056480493 0.26265625

0.6 0.0625 0.25

0.61 0.068988306 0.23765625

0.62 0.075969141 0.225625

0.63 0.083466821 0.21390625

0.64 0.09150625 0.2025

0.65 0.100112915 0.19140625

0.66 0.109312891 0.180625

0.67 0.119132837 0.17015625

0.68 0.1296 0.16

0.69 0.140742212 0.15015625

0.7 0.152587891 0.140625

0.71 0.16516604 0.13140625

0.72 0.17850625 0.1225

0.73 0.192638696 0.11390625

0.74 0.207594141 0.105625

0.75 0.223403931 0.09765625

0.76 0.2401 0.09

0.77 0.257714868 0.08265625

0.78 0.276281641 0.075625

0.79 0.295834009 0.06890625

0.8 0.31640625 0.0625

0.81 0.338033228 0.05640625

0.82 0.360750391 0.050625

0.83 0.384593774 0.04515625

0.84 0.4096 0.04

0.85 0.435806274 0.03515625

0.86 0.463250391 0.030625

0.87 0.491970728 0.02640625

0.88 0.52200625 0.0225

0.89 0.553396509 0.01890625

0.9 0.586181641 0.015625

0.91 0.620402368 0.01265625

0.92 0.6561 0.01

0.93 0.693316431 0.00765625

0.94 0.732094141 0.005625

0.95 0.772476196 0.00390625

0.96 0.81450625 0.0025

0.97 0.85822854 0.00140625

0.98 0.903687891 0.000625

0.99 0.950929712 0.00015625

1 1 0

** ---------- INITIAL CONDITIONS ----------

INITIAL

USER_INPUT

PRES CON 9000

SW CON 1

ZGLOBALC 'CO2' CON 0

ZGLOBALC 'NC10' CON 1

*MOLALITY-AQUEOUS 0.0

** ---------- NUMERICAL CONTROL ----------

```
NUMERICAL
DTMAX 0.0001
CONVERGE MAXRES TIGHT



** ------------------------------------ RECURRENT DATA -----------------------------------------


RUN
Time 0
DTWELL 0.01
DTMIN 0.00001
AIMWELL WELLN



WELL  'CO2-INJ'
**     Solvent Injection (mole fraction)        ** All rates 120  180  240 mL/h
      **<-------- 1 to Nc ------------>
INJECTOR 'CO2-INJ'
INCOMP  SOLVENT  1.0  0.0
OPERATE  MAX  BHG  0.000288  CONT
**         rad  geofac  wfrac  skin
GEOMETRY  I  0.001  0.37  1.0  0.0
     PERF      GEOA  'CO2-INJ'
** UBA             ff         Status  Connection
   50 1 1        1.0  OPEN    FLOW-FROM  'SURFACE'

**
WELL  'SURF-INJ'
**    Inject water along with surfactant (0.0 molality)
```

```
      **<-- 1 to Nc --> <--Surf-->
INJECTOR 'SURF-INJ'
INCOMP  AQUEOUS  0.0  0.0  0.0247

OPERATE  MAX  STW  0.002592  CONT
**        rad  geofac  wfrac  skin
GEOMETRY  I  0.001  0.37  1.0  0.0
    PERF     GEOA  'SURF-INJ'
** UBA           ff        Status  Connection
  50 1 1       1.0  OPEN    FLOW-FROM  'SURFACE'

**
WELL 'PROD'
**
PRODUCER 'PROD'
OPERATE  MIN  BHP  9000.0  CONT
**        rad  geofac  wfrac  skin
GEOMETRY  I  0.001  0.37  1.0  0.0
    PERF     GEOA  'PROD'
** UBA           ff        Status  Connection
  1 1 1       1.0  OPEN    FLOW-TO  'SURFACE'

TIME    0.01
TIME    0.026579
TIME    0.15947
** 180 mL/h ***********************************
INJECTOR 'CO2-INJ'
INCOMP  SOLVENT  1.0  0.0
OPERATE  MAX  BHG  0.000432  CONT
INJECTOR 'SURF-INJ'
INCOMP  AQUEOUS  0.0  0.0  0.0247
```

```
OPERATE  MAX  STW  0.003888  CONT

TIME     0.19491
** 240 mL/h  **********************************
INJECTOR 'CO2-INJ'
INCOMP  SOLVENT  1.0  0.0
OPERATE  MAX  BHG  0.000576  CONT
INJECTOR 'SURF-INJ'
INCOMP  AQUEOUS  0.0  0.0  0.0247

OPERATE  MAX  STW  0.005184  CONT

TIME     0.22149

STOP
```

References

Abou-Kassem, J. H., Islam, M. R. and Farouq-Ali, S. M. (2013) *Petroleum Reservoir Simulations*. Elsevier. doi: https://doi.org/10.1016/B978-0-9765113-6-6.50007-1.

Ahmadi, M. A., Pouladi, B. and Barghi, T. (2016) 'Numerical modeling of CO2injection scenarios in petroleum reservoirs: Application to CO2sequestration and EOR', *Journal of Natural Gas Science and Engineering*. Elsevier B.V, 30, pp. 38–49. doi: 10.1016/j.jngse.2016.01.038.

Alcorn, Z. P. (2018) *Upscaling CO 2 Foam for Enhanced Oil Recovery and CO 2 Storage from Laboratory to Field Scale An Integrated Approach to Designing a Field Pilot Test*. University of Bergen.

Alvarado, V. and Manrique, E. (2010) 'Enhanced oil recovery: An update review', *Energies*, 3(9), pp. 1529–1575. doi: 10.3390/en3091529.

Archer, J. S. and Wall, C. G. (2012) *Petroleum engineering: principles and practice*. Springer Science & Business Media.

Bachu, S. and Adams, J. J. (2003) 'Sequestration of CO2 in geological media in response to climate change: capacity of deep saline aquifers to sequester CO2 in solution', *Energy Conversion and management*. Elsevier, 44(20), pp. 3151–3175.

Bahadori, A. (2018) *Fundamentals of Enhanced Oil and Gas Recovery from Conventional and Unconventional Reservoirs*. Oxford, UK: Elsevier.

Baker, R. O. *et al.* (2006) 'History matching standards; quality control and risk analysis for simulation', *Canadian International Petroleum Conference*. Petroleum Society of Canada. doi: https://doi.org/10.2118/2006-129.

Bennetzen, M. V. and Mogensen, K. (2014) 'Novel Applications of Nanoparticles for Future Enhanced Oil Recovery', *International Petroleum Technology Conference*, (December), pp. 10–12. doi: 10.2523/IPTC-17857-MS.

Bennion, D. B. and Bachu, S. (2010) 'Drainage and Imbibition CO2/Brine Relative Permeability Curves at Reservoir Conditions for High-Permeability Carbonate Rocks', *SPE Annual Technical Conference and Exhibition*, pp. 1–18. doi: 10.2118/134028-MS.

Berg, J. C. (2010) *An introduction to interfaces & colloids: the bridge to nanoscience*. World Scientific.

Bertin, H. J., Quintard, M. Y. and Castanier, L. M. (1998) 'Development of a Bubble-Population Correlation for Foam-Flow Modeling in Porous Media', *SPE Journal*, 3(04), pp. 356–362. doi: 10.2118/52596-PA.

Blunt, M., Fayers, F. J. and Orr, F. M. (1993) 'Carbon dioxide in enhanced oil recovery', *Energy Conversion and Management*, 34(9–11), pp. 1197–1204. doi: 10.1016/0196-8904(93)90069-M.

Chang, S.-H. and Grigg, R. B. (1999) 'Effects of Foam Quality and Flow Rate on CO2-Foam Behavior at Reservoir Temperature and Pressure', *SPE Reservoir Evaluation & Engineering*, 2(03), pp. 248–254. doi: 10.2118/56856-PA.

Chen, Q., Gerritsen, M. and Kovscek, A. R. (2010) 'Modeling Foam Displacement With the Local-Equilibrium Approximation: Theory and Experimental Verification', *SPE Journal*, 15(01), pp. 171–183. doi: 10.2118/116735-PA.

Computer Modelling Group Ltd (2016) *CMG User's Guide*. Calgary, Canada.

Computer Modelling Group Ltd (2017) *CMG User's Guide*. Calgary, Canada.

Corey, A. T. (1954) 'The interrelation between gas and oil relative permeabilities', *Producers Monthly*, pp. 38–41.

David, A. and Marsden Jr, S. S. (1969) 'The rheology of foam', *Fall Meeting of the Society of Petroleum Engineers of AIME*. Society of Petroleum Engineers. doi: https://doi.org/10.2118/2544-MS.

Dicksen, T., Hirasaki, G. J. and Miller, C. A. (2002) 'Conditions for Foam Generation in Homogeneous Porous Media', *SPE/DOE Improved Oil Recovery Symposium*. doi: 10.2118/75176-MS.

Do, H. D. and Pinczewski, W. V. (1993) 'Diffusion-controlled swelling of reservoir oil by indirect contact with injection gas', *Chemical Engineering Science*, 48(18), pp. 3243–3252. doi: 10.1016/0009-2509(93)80208-8.

Doughty, C. (2005) 'Flow Modeling for CO2 Sequestration : The Frio Brine Pilot'. Califorina, USA: The American Geophysical Union Fall Meeting, pp. 1–2.

Doyle, G., Orr, F. M. (2018) 'Carbon capture, Utilization, and storage (CCUS) - an update', *SPE*. Stanford, CA, USA: SPE, (December). doi: 10.1049/iet-tv.50.15777.

Enick, R. M. *et al.* (2012) 'Mobility and Conformance Control for CO2 EOR via Thickeners, Foams, and Gels -- A Literature Review of 40 Years of Research and Pilot Tests', *SPE Improved Oil Recovery Symposium*. Oklahoma, USA, (14–18 April), pp. 1–12. doi: 10.2118/154122-MS.

EPA (2018) 'Inventory of U . S . Greenhouse Gas Emissions and Sinks'. Washington, USA: The United States Environmental Protection Agency (EPA), 4(1), pp. 9–13.

Equinor (2019) *Energy Perspectives, Long-term macro and market outlook*. Stavanger.

Ettinger, R. A. and Radke, C. J. (1992) 'Influence of Texture on Steady Foam Flow in Berea Sandstone', *SPE Reservoir Engineering*, 7(01), pp. 83–90. doi: 10.2118/19688-PA.

Exxon Mobil (2019) *Carbon Capture and Sequestration [Online]. Available: https://cdn.exxonmobil.com/~/media/global/images/inline-images/graphics/carbon-capture-and-sequestration_article-image-jpg.jpg?as=1*.

Fanchi, J. R. (2005) *Principles of applied reservoir simulation*. Elsevier.

Farajzadeh, R. *et al.* (2012) 'Foam-oil interaction in porous media: Implications for foam assisted enhanced oil recovery', *Advances in Colloid and Interface Science*. Elsevier B.V., 183–184, pp. 1–13. doi: 10.1016/j.cis.2012.07.002.

Farajzadeh, R. *et al.* (2015) 'Effect of permeability on implicit-texture foam model parameters and the limiting capillary pressure', *Energy & fuels*. ACS Publications, 29(5), pp. 3011–3018.

Farajzadeh, R., Andrianov, A. and Zitha, P. L. J. (2010) 'Investigation of immiscible and miscible foam for enhancing oil recovery', *Industrial and Engineering Chemistry Research*, 49(4), pp. 1910–1919. doi: 10.1021/ie901109d.

Fredriksen, S. B. (2018) *The Use of CO 2 Foam Mobility Control for Enhanced Oil Recovery and Associated CO 2 Storage A Multi-Scale Approach for Lab-to-Field Applications*. University of Bergen.

Friedmann, F., Chen, W. H. and Gauglitz, P. A. (1991) 'Experimental and Simulation Study of High-Temperature Foam Displacement in Porous Media', *SPE Reservoir Engineering*, 6(01), pp. 37–45. doi: 10.2118/17357-PA.

Friedmann, F. and Jensen, J. A. (1986) 'Some Parameters Influencing the Formation and Propagation of Foams in Porous Media', *SPE California Regional Meeting*. doi: 10.2118/15087-MS.

Gao, C. (2007) 'Factors affecting particle retention in porous media', *Emirates Journal for Engineering*

Research, 12(3), pp. 1–7.

Gauglitz, P. A. *et al.* (2002) 'Foam Generation in Porous Media', *Society of Petroleum Engineers*. doi: https://doi.org/10.2118/75177-MS.

Gauteplass, J. *et al.* (2015) 'Pore-level foam generation and flow for mobility control in fractured systems', *Colloids and Surfaces A: Physicochemical and Engineering Aspects*. Elsevier B.V., 468, pp. 184–192. doi: 10.1016/j.colsurfa.2014.12.043.

Green, D. W. and Willhite, G. P. (1998) 'Enhanced oil recovery', in. Henry L. Doherty Memorial Fund of AIME, Society of Petroleum Engineers ….

Hardisty, P. E., Sivapalan, M. and Brooks, P. (2011) 'The environmental and economic sustainability of carbon capture and storage', *International Journal of Environmental Research and Public Health*, 8(5), pp. 1460–1477. doi: 10.3390/ijerph8051460.

Hasan, M. M. F. *et al.* (2015) 'A multi-scale framework for CO2 capture, utilization, and sequestration: CCUS and CCU', *Computers & Chemical Engineering*. Elsevier, 81, pp. 2–21. doi: 10.1016/j.compchemeng.2015.04.034.

Hassan, H. *et al.* (2018) 'Gearing Toward CCUS for CO2 Reduction in Malaysia', *Offshore Technology Conference Asia*. Kuala Lumpur, Malaysia: Offshore Technology Conference, p. 4. doi: 10.4043/28408-MS.

Hirasaki, G. *et al.* (2015) *Novel CO 2 Foam Concepts and Injection Schemes for Improving CO 2 Sweep Efficiency in Sandstone and Carbonate Hydrocarbon Formations Final Technical Report Report Date : February 5 , 2015 Principal Investigator : Quoc P . Nguyen Department of Petroleum &*. Texas, USA: The U.S. Department of Energy / National Energy Technology Laboratory under Award Number DE-FE0005902.

Hirasaki, G. J. and Lawson, J. B. (1985) 'Mechanisms of Foam Flow in Porous Media: Apparent Viscosity in Smooth Capillaries', *Society of Petroleum Engineers Journal*. Society of Petroleum Engineers, 25(02), pp. 176–190. doi: 10.2118/12129-PA.

Holm, L. W. (1986) 'Miscibility and Miscible Displacement'. Society of Petroleum Engineers Jurnal, 38(August), pp. 817–818. doi: 10.2118/15794-PA.

Holm, L. W. and Josendal, V. A. (1974) 'Mechanisms of Oil Displacement By Carbon Dioxide', *Journal of Petroleum Technology*, 26(12), pp. 1427–1438. doi: 10.2118/4736-PA.

IPCC (2016) 'Inventory of U . S . Greenhouse Gas Emissions and Sinks : 1990 – 2014', in *Ipcc*. doi: EPA 430-R-13-001.

Kamali, F. *et al.* (2015) 'Study of Co-Optimizing CO2 Storage and CO2 Enhanced Oil Recovery', (December), pp. 1–11. doi: 10.2118/171520-PA.

Khajehpour, M. *et al.* (2016) 'Nanoparticles as Foam Stabilizer for Steam-Foam Process', *SPE EOR Conference at Oil and Gas West Asia*. Muscat, Oman: Society of Petroleum Engineers, p. 14. doi: 10.2118/179826-MS.

Kim, J., Dong, Y. and Rossen, W. R. (2005) 'Steady-State Flow Behavior of CO2 Foam', *SPE Journal*, 10(04), pp. 405–415. doi: 10.2118/89351-PA.

Kim, J. S., Dong, Y. and Rossen, W. R. (2005) 'Steady-state flow behavior of CO<inf>2</inf>foam', *SPE Journal*, 10(4), pp. 405–415. doi: 10.2118/89351-PA.

Kokal, S. and Al-Kaabi, A. (2010) 'Enhanced oil recovery: challenges & opportunities', *World Petroleum Council: Official Publication*, 64, pp. 64–69.

Kovscek, A. R. and Radke, C. J. (1994) 'Fundamentals of foam transport in porous media', *ACS Advances in Chemistry Series*. ACS Publications, 242, pp. 115–164. doi: 10.1021/ba-1994-0242.ch003.

Lake, L. W. *et al.* (2014) *Fundamentals of enhanced oil recovery*. Texas: Society of Petroleum Engineers Richardson.

Lee, H. O., Heller, J. P. and Hoefer, A. M. W. (1991) 'Change in Apparent Viscosity of CO2 Foam With Rock Permeability', *SPE Reservoir Engineering*, 6(04), pp. 421–428. doi: 10.2118/20194-PA.

Lee, S. and Kam, S. I. (2013) *Chapter 2 - Enhanced Oil Recovery by Using CO2 Foams: Fundamentals and Field Applications*. First Edit. Elsevier Inc. doi: 10.1016/B978-0-12-386545-8.00002-6.

Leung, D. Y. C., Caramanna, G. and Maroto-Valer, M. M. (2014) 'An overview of current status of carbon dioxide capture and storage technologies', *Renewable and Sustainable Energy Reviews*. Elsevier, 39, pp. 426–443. doi: 10.1016/j.rser.2014.07.093.

Liontas, R. *et al.* (2013) 'Neighbor-induced bubble pich-off: Novel mechanisms of in situ foam generation in microfluidic channels', *Soft Matter*, 9(46), pp. 10971–10984. doi: 10.1039/c3sm51605a.

Liu, M., Andrianov, A. and Rossen, W. R. (2011) 'Sweep Efficiency in CO2 Foam Simulations with Oil', *SPE EUROPEC/EAGE Annual Conference and Exhibition*. Vienna, Austria, (23–26 May), pp. 1–18. doi: 10.2118/142999-MS.

Ma, K., Farajzadeh, R., *et al.* (2013) 'Estimation of Parameters for the Simulation of Foam Flow through Porous Media: Part 3; Non-Uniqueness, Numerical Artifact and Sensitivity', pp. 1–20. doi: 10.2118/165263-ms.

Ma, K., Lopez-Salinas, J. L., *et al.* (2013) 'Estimation of parameters for the simulation of foam flow through porous media. Part 1: The dry-out effect', *Energy and Fuels*, 27(5), pp. 2363–2375. doi: 10.1021/ef302036s.

Mattax, C. C. and Dalton, R. L. (1990) 'Reservoir Simulation (includes associated papers 21606 and 21620)', *Journal of Petroleum Technology*. Society of petroleum engineers, 42(06), pp. 692–695.

Metin, C. O. *et al.* (2011) 'Stability of aqueous silica nanoparticle dispersions', *Journal of Nanoparticle Research*, 13(2), pp. 839–850. doi: 10.1007/s11051-010-0085-1.

Mo, D. *et al.* (2012) 'Study of the Effect of Different Factors on Nanoparticle-Stablized CO2 Foam for Mobility Control', *SPE Annual Technical Conference and Exhibition*. doi: 10.2118/159282-MS.

Mo, D. *et al.* (2014) 'Study Nanoparticle-stabilized CO2 Foam For Oil Recovery At Different Pressure, Temperature, And Rock Samples', *SPE Improved Oil Recovery Symposium*, pp. 1–11. doi: 10.2118/169110-MS.

Mosavat, N., Abedini, A. and Torabi, F. (2014) 'Phase Behaviour of CO2-Brine and CO2-oil systems for CO2 storage and enhanced oil recovery: Experimental studies', *Energy Procedia*. Elsevier B.V., 63, pp. 5631–5645. doi: 10.1016/j.egypro.2014.11.596.

Munro, D. R. *et al.* (2016) 'Global carbon budget 2016', *Earth System Science Data*, 8(2). doi: https://doi.org/10.5194/essd-8-605-2016.

Negin, C., Ali, S. and Xie, Q. (2016) 'Application of nanotechnology for enhancing oil recovery – A review', *Petroleum*. Elsevier Ltd, 2(4), pp. 324–333. doi: 10.1016/j.petlm.2016.10.002.

Ogolo, N. A. *et al.* (2012) 'Spe-160847-Ms'. doi: 10.2118/160847-MS.

Panuganti, S. R. *et al.* (2012) 'PC-SAFT characterization of crude oils and modeling of asphaltene phase behavior', *Fuel*. Elsevier Ltd, 93, pp. 658–669. doi: 10.1016/j.fuel.2011.09.028.

Pope, G. A. (2011) 'Recent Developments and Remaining Challenges of Enhanced Oil Recovery.', *Journal of Petroleum Technology*, (July), pp. 65–68. doi: https://doi.org/10.2118/0711-0065-JPT.

Pruess, K. *et al.* (2001) 'Numerical modeling of aquifer disposal of CO2', in *SPE/EPA/DOE Exploration and Production Environmental Conference*. San Antonio, Texas: Society of Petroleum Engineers. doi: https://doi.org/10.2118/66537-MS.

Ransohoff, T. C. and Radke, C. J. (1988) 'Mechanisms of Foam Generation in Glass-Bead Packs', *SPE Reservoir Engineering*, 3(02), pp. 573–585. doi: 10.2118/15441-PA.

Rognmo, A. U. (2019) *CO2 -Foams for Enhanced Oil Recovery and CO2 Storage*. University of Bergen.

Rognmo, A. U., Horjen, H. and Fernø, M. A. (2017) 'Nanotechnology for improved CO2utilization in CCS: Laboratory study of CO2-foam flow and silica nanoparticle retention in porous media', *International Journal of Greenhouse Gas Control*. Elsevier, 64(March), pp. 113–118. doi: 10.1016/j.ijggc.2017.07.010.

Rossen, W. R. (1996) *Foams in enhanced oil recovery*, *Foams: Theory, Measurements and Applications*. Marcel Dekker, New York.

Rossen, W. R. *et al.* (2007) 'Gravity Segregation in Gas-Injection IOR', *Technology*. London, UK: Society of Petroleum Engineers, (11–14 June), pp. 1–10. doi: 10.2118/107262-MS.

Rossen, W. R. R. (1999) 'Foam Generation at Layer Boundaries in Porous Media', *SPE Journal*, 4(04), pp. 409–412. doi: 10.2118/59395-PA.

Schramm, L. L. (1994) 'Foam sensitivity to crude oil in porous media', *ACS Advances in Chemistry Series*. Washington, DC: American Chemical Society,[1950]-, 242, pp. 165–200.

Schramm, L. L. (1994) *Foams: fundamentals and applications in the petroleum industry*. An American Chemical Society Publication.

Sheng, J. J. (2013a) *Foams and Their Applications in Enhancing Oil Recovery*. First Edit, *Enhanced Oil Recovery Field Case Studies*. First Edit. Elsevier Inc. doi: 10.1016/B978-0-12-386545-8.00011-7.

Sheng, J. J. (2013b) *Surfactant Enhanced Oil Recovery in Carbonate Reservoirs*. First Edit, *Enhanced Oil Recovery Field Case Studies*. First Edit. Elsevier Inc. doi: 10.1016/B978-0-12-386545-8.00012-9.

Skauge, T., Spildo, K. and Skauge, A. (2010) 'Nano-sized Particles For EOR', *SPE Improved Oil Recovery Symposium*, (April), pp. 24–28. doi: 10.2118/129933-MS.

Skjæveland, SM and Kleppe, J. (1992) 'Recent Advances in Improved Oil Recovery Methods for North Sea Sandstone Reservoirs', *Norwegian Petroleum Directorate, Stavanger*, (December 2016), pp. 207–238. doi: 10.1039/c5ra01934f.

Steeneveldt, R., Berger, B. and Torp, T. A. (2006) 'CO2 capture and storage: closing the knowing–doing gap', *Chemical Engineering Research and Design*. Elsevier, 84(9), pp. 739–763.

Sun, L. *et al.* (2019) 'Recent advances of surfactant-stabilized N2/CO2 foams in enhanced oil recovery', *Fuel*. Elsevier, 241(September 2018), pp. 83–93. doi: 10.1016/j.fuel.2018.12.016.

Svorstol, I., Vassenden, F. and Mannhardt, K. (1996) 'Laboratory Studies for Design of a Foam Pilot in the Snorre Field', *SPE/DOE Improved Oil Recovery Symposium*, pp. 1–11. doi: 10.2118/35400-MS.

UNFCC (2015) *Synthesis report on the aggregate effect of the intended nationally determined contributions.* Available at: http://unfccc.int/focus/indc_portal/items/9240.php.

Wang, S. *et al.* (2018) 'In-situ CO2generation for EOR by using urea as a gas generation agent', *Fuel*, 217(December 2017), pp. 499–507. doi: 10.1016/j.fuel.2017.12.103.

Wei, B. *et al.* (2017) 'Interactions and phase behaviors between oleic phase and CO2 from swelling to miscibility in CO2-based enhanced oil recovery (EOR) process: A comprehensive visualization study', *Journal of Molecular Liquids*. Elsevier B.V., 232, pp. 277–284. doi: 10.1016/j.molliq.2017.02.090.

Yellig, W. F. and Metcalfe, R. S. (1980) 'Determination and Prediction of CO 2 Minimum Miscibility Pressures', *Journal of Petroleum Technology*, pp. 160–168. doi: 10.2118/7477-PA.

Yu, J. *et al.* (2012) 'Foam Mobility Control for Nanoparticle-Stabilized CO 2 Foam', *SPE Improved Oil Recovery Symposium*, pp. 1–13. doi: 10.2118/153336-ms.

Zhang, H., Hou, D. and Li, K. (2015) 'An Improved CO2-Crude Oil Minimum Miscibility Pressure Correlation', *Journal of Chemistry*. Sichuan, China, (11 October). doi: 10.1155/2015/175940.

Zhang, N. *et al.* (2019) 'Identification of CO2 sequestration opportunities: CO2 miscible flooding guidelines', *Fuel*. Elsevier, 241(December 2018), pp. 459–467. doi: 10.1016/j.fuel.2018.12.072.

Zhang, T. *et al.* (2009) 'Foams and Emulsions Stabilized With Nanoparticles for Potential Conformance Control Applications', *SPE International Symposium on Oilfield Chemistry*. doi: 10.2118/121744-MS.

Zhang, T. *et al.* (2010) 'Nanoparticle-Stabilized Emulsions for Applications in Enhanced Oil Recovery', *SPE Improved Oil Recovery Symposium*. doi: 10.2118/129885-MS.

Zolotukhin, A. B. and Ursin, J.-R. (2000) *Introduction to petroleum reservoir engineering*. 1 ed. Kristiansand, Norway: Norwegian Academic Press (HóyskoleForlaget).